Preprint: The acoustic impedance of three-dimensional turbines

James Brind

Whittle Laboratory, University of Cambridge
1 JJ Thomson Avenue, Cambridge, CB3 0DY, UK

Abstract

Thermoacoustic stability assessment of gas turbine combustors requires an acoustic impedance boundary condition for the downstream turbomachinery. Actuator disk type analytical methods offer rapid predictions of acoustic impedance in an iterative design process; previous studies show that this class of models works well for cascades consistent with a two-dimensional assumption. Real turbines, however, are three-dimensional with multiple stages, coolant flows, and leakage flows. The first part of this paper validates a cambered semi-actuator disk model for the acoustic impedance of a realistic multi-stage turbine using non-linear time-marching computations: the two methods agree to within 9% for incident pressure waves and 14% for incident entropy waves. Simulations of the multi-stage turbine with different inlet conditions confirm that, to a close approximation, inlet corrected flow and hence Mach numbers and acoustic impedance are constant during off-design operation. The second part of the paper then applies both analytical and computational approaches to families of parametrically generated turbine stages to quantify three-dimensional design effects. The results show that the influence of hub-to-tip ratio on acoustic impedance is weak, and the two-dimensional analytical model is accurate even for high aspect ratio stages. Front-loaded camber lines increase axial Mach number within blade passages, raising acoustic impedance by up to 51% compared to a datum quadratic camber line. Varying the stator–rotor axial gap changes the relative phase of reflections from vanes and blades, causing the total impedance to either increase or decrease, at different frequencies, by up to 11%. The cambered semi-actuator disk method consistently captures the correct trends, showing that the physical basis of the model is sufficient to produce a broadly applicable tool for rapid assessment of turbine impedance boundary conditions.

Keywords: turbine, impedance, aeroacoustics, thermoacoustic stability

Email address: jb753@cam.ac.uk (James Brind)

Nomenclature

Latin

a	Acoustic wave speed [$\mathrm{m\,s^{-1}}$]
$\mathcal{A}$	Aft-loading factor [–], Eqn. (14)
c_x	Vane axial chord [m]
f	Frequency [Hz]
g	Stator–rotor axial gap [m]
HTR	Hub-to-tip radius ratio [–]
i	Imaginary unit [–]
Ma	Mach number [–]
p	Pressure [Pa]
r	Radial coordinate [m]
$\mathcal{R}$	Reflection coefficient [–]
Re	Reynolds number [–]
s	Entropy [$\mathrm{J\,kg^{-1}\,K^{-1}}$]
t	Time [s]
T	Temperature [K]
$\mathcal{T}$	Transmission coefficient [–]
U	Rotor blade speed [$\mathrm{m\,s^{-1}}$]
V	Velocity [$\mathrm{m\,s^{-1}}$]
x	Axial coordinate [m]

Greek

α	Flow yaw angle [°]
γ	Ratio of specific heats [–]
Γ	Turbine inlet corrected flow [–], Eqn. (13)
κ	Reduced frequency [–], Eqn. (1)
θ	Circumferential coordinate [rad]
Θ	Normalised inlet stagnation temperature [–], Eqn. (11)
ρ	Density [$\mathrm{kg\,m^{-3}}$]
υ	Vorticity [$\mathrm{s^{-1}}$]
Φ	Normalised inlet mass flow [–], Eqn. (12)
χ	Camber line angle [°]

Subscripts and accents

$\square_0$	Stagnation state
$\square_\mathrm{d}$	Design point value
$\square_\mathrm{in}$	Turbine inlet plane
$\square_\mathrm{out}$	Turbine outlet plane
$\square'$	Perturbation about time average
$\widehat{\square}$	Characteristic wave
$\square^+$	Downstream-propagating
$\square^-$	Upstream-propagating

Abbreviations

CFD	Computational Fluid Dynamics
TAD	Turbine Actuator Disk (analytical model)

1. Introduction

In gas turbine combustors, thermoacoustic instability occurs when acoustic resonance of the combustion chamber couples with perturbations to fuel heat release rate. If acoustic pressure and heat release perturbations are in phase, unsteady combustion acts as a source of acoustic energy. If energy input exceeds losses through the boundaries of the system, and due to damping devices, self-excited thermoacoustic oscillations will grow to high amplitudes (Dowling [1]). In benign cases, thermoacoustic instability leads to increased noise levels; in severe cases, thermoacoustic instability causes mechanical damage and halts operation of the turbine.

Predicting thermoacoustic instability requires a model for the acoustic behaviour of the combustor, including accurate boundary conditions at the connections to compressor and turbine. The boundary conditions may be expressed as acoustic impedances, which quantify the amplitude and phase of waves reflected from the boundaries (equivalently, loss of acoustic energy through the boundaries). According to Poinsot [2], applying correct impedance boundary conditions is a key issue when predicting the stability of real combustion systems, as opposed to laboratory-scale rigs where the boundary conditions are simple and well-characterised.

This paper considers impedances for both incident pressure and entropy waves, because reflections can arise from either 'direct' or 'indirect' noise (Dowling and Mahmoudi [3], Ihme [4]). Direct noise is pressure fluctuations created by the combustion reaction. Indirect noise is produced by the interaction of flow inhomogeneities, such as temperature hot spots, with an accelerating mean flow through the turbine.

During a gas turbine development process, rapid assessment of acoustic impedance with each turbine design iteration facilitates identifying and avoiding combustion system instability at an early stage. Alternatively, Juniper and Sujith [5] argue that given the extreme sensitivity of thermoacoustic stability to design parameters, small changes after a full engine test are sufficient to eliminate instability. A computationally inexpensive model for turbine impedance allows quick examination of many possible modifications.

Actuator-disk type methods are one way of predicting turbine acoustic impedance, based on analytical solutions of the two-dimensional linearised Euler equations. First, Marble and Candel [6] proposed the approach for quasi-one-dimensional nozzles, then Cumpsty and Marble [7] extended the method to two dimensions. The basic actuator disk model is valid in the low-frequency limit where blade rows become compact discontinuities in mean flow. Applying conservation of perturbation mass flux, energy, and entropy across a row yields a set of four simultaneous linear equations in terms of characteristic waves, encapsulating the acoustic behaviour of each blade row.

Leyko et al. [8] and Mishra and Bodony [9] compared the Cumpsty and Marble [7] actuator disk theory to non-linear time-marching computations of two-dimensional turbine stators. Bauerheim et al. [10] extended the validation of Leyko et al. [8] to a two-dimensional turbine stage. These studies found that actuator disk predictions match computational fluid dynamics (CFD) results to within of order 10% impedance magnitude at low reduced frequencies $\kappa \leq 0.05$, where this paper defines reduced frequency,

$$\kappa = f c_x / a \,. \tag{1}$$

The actuator disk approach is inaccurate at higher frequencies due to non-compact effects.

The semi-actuator disk theory, after Kaji and Okazaki [11], treats blade rows as a cascade of flat plates with finite chord, allowing a propagation time for waves to move axially through the row. The formulation neglects pitchwise non-compact effects, but Kaji and Okazaki [12] found this to be an adequate approximation under conditions typical of axial compressors.

Brind and Pullan [13] extended the semi-actuator disk theory to cambered turbine blades, by discretising the chord into multiple flat-plate elements. Capturing axially non-uniform flow within a cambered blade row gives a better estimate of wave propagation time for such geometries. For a two-dimensional turbine stage, comparing the cambered semi-actuator disk model with time-marching CFD gave agreement to within 16% impedance magnitude across the entire reduced frequency range $\kappa \leq 0.1$ representative of thermoacoustic instability.

The cited studies show that actuator-disk type models work well in idealised cases that are consistent with their assumptions — but, real turbines are not two-dimensional. At low hub-to-tip radius ratios, radial equilibrium requires twisted blades to maintain constant axial velocity. Endwall boundary layers, growing throughout multi-stage turbines, and three-dimensional vane or blade geometry also cause radial non-uniformity.

The only reported comparison of actuator-disk theory with three-dimensional CFD is that of Papadogiannis et al. [14], considering a single-stage turbine. They report results at a single frequency $\kappa = 0.1$ for entropy wave excitation. The theory gives a good prediction of downstream-running entropy noise, but the upstream-running entropy noise is over-predicted by a factor of 4.6 compared to the CFD. These data are not sufficient to confirm the general validity of two-dimensional analytical models to predict impedance of real three-dimensional multi-stage turbines.

In practical applications, gas turbines are often operated away from their specified design point, which may trigger thermoacoustic instability [5]. In general, the turbine flow field will be different from nominal conditions, hence the acoustic impedance may change. Analysis of off-design thermoacoustic instability would then require updated turbine impedance boundary conditions.

Brind and Pullan [13] considered the effect of mean-line turbine design on acoustic impedance, finding that flow coefficient was the most influential one-dimensional parameter. With three-dimensional turbines, there are extra degrees of freedom available to the designer: geometry changes that affect the detail of the flow field while maintaining the same mean-line aerodynamics. In particular, this paper considers such changes to hub-to-tip radius ratio, chordwise loading distribution, and stator–rotor axial gap, illustrated graphically in Fig. 1.

The present work uses a combination of the cambered semi-actuator disk analytical model and time-marching CFD results to quantify acoustic impedance of three-dimensional turbines, answering the following research questions:

- What are the modelling requirements for predicting acoustic impedance of realistic three-dimensional multi-stage turbines, and, specifically, is a two-dimensional semi-actuator disk model sufficient?
- Does off-design operation have an effect on multi-stage turbine acoustic impedance?
- Which three-dimensional design parameter has the most influence on on turbine stage impedance: hub-to-tip ratio, loading distribution, or stator–rotor axial gap?

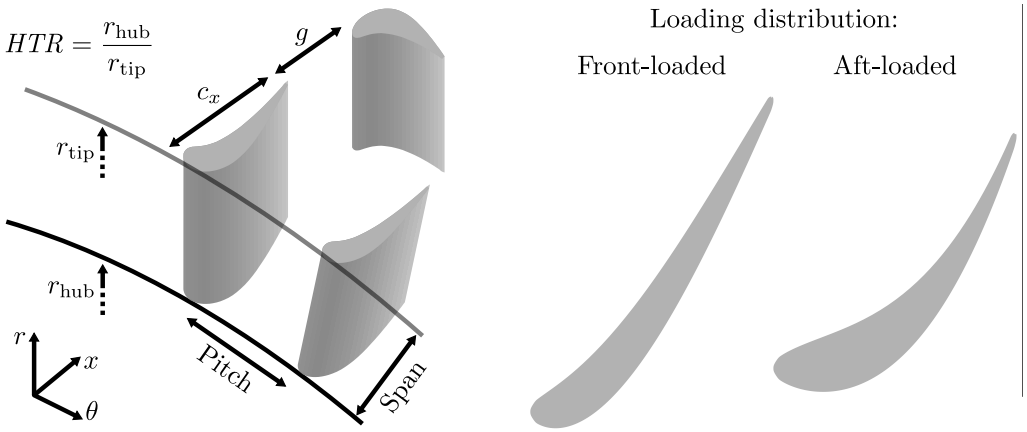

Figure 1: Three-dimensional design parameters considered in this study: hub-to-tip radius ratio, *HTR*; chordwise loading distribution; stator–rotor axial gap g/c_x.

2. Cambered semi-actuator disk analytical model

This section describes an analytical model for predicting turbine acoustic impedance, an extension of the actuator and semi-actuator disk models. The model is named TAD for short, after "Turbine Actuator Disk". Cumpsty and Marble [7] and Bauerheim et al. [10] give full derivations of the actuator disk approach, which assumes blade rows to be compact and models them as discontinuities in the mean flow. Kaji and Okazaki [11] relaxed the assumption of axial compactness in their semi-actuator disk approach, by modelling blade rows as a cascade of flat plates. Brind and Pullan [13] introduced an extension to cambered blades, by discretising along the chord into a series of coupled semi-actuator disks. Figure 2 illustrates the different levels of modelling fidelity.

An acoustic model for a turbomachine must capture two processes: the propagation of waves in open annulus, and the interaction between waves and blade rows. The remainder of this section addresses each process in turn to assemble a system of governing equations, and then describes a method for their solution.

2.1. Wave propagation in annular geometries

The model splits a turbine into control volumes representing the inlet, outlet, and spaces between blade rows, Fig. 3. The mean flow in each control volume is uniform and steady; for the present work, two-dimensional axial cuts from RANS CFD solutions, mixed out at constant area to a uniform state, are used to prescribe the mean flow field. Appendix A specifies the mixing process. Unsteady, non-uniform perturbations about the mean flow obey the two-dimensional linearised Euler equations under the assumptions of: (a) small-amplitude perturbations, (b) high hub-to-tip radius ratio, and (c) high Reynolds number. The assumptions permit the neglect of second-order terms, spanwise variations in mean flow, and viscous or heat conduction effects. For the industrially relevant cases in this paper, axial Mach numbers are subsonic.

There is a classical analytical solution for wave propagation in annular geometries. At the low frequencies representative of combustion instability, only plane waves propagate.

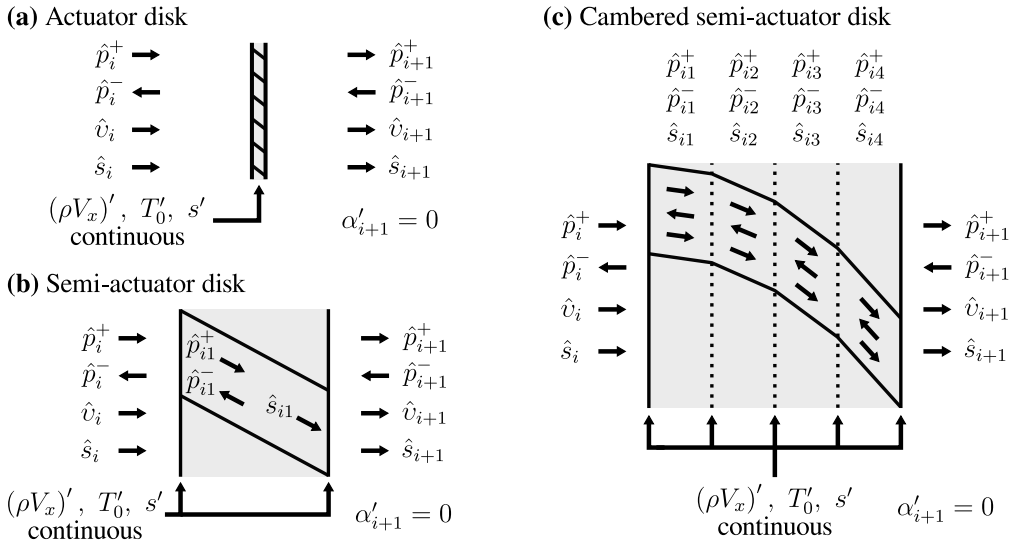

Figure 2: Blade row models for determining acoustic impedance: actuator disk, after Cumpsty and Marble [7]; semi-actuator disk, after Kaji and Okazaki [11]; cambered semi-actuator disk. From Brind and Pullan [13].

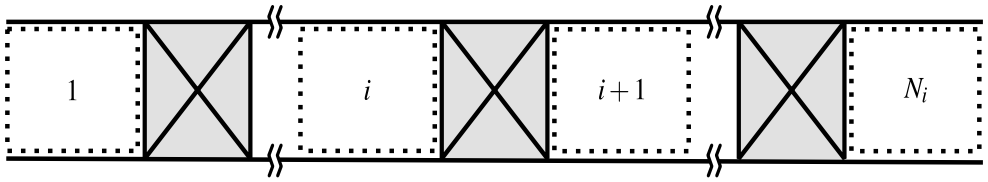

Figure 3: Control volumes for Turbine Actuator Disk analytical model. From Brind and Pullan [13]

Seeking solutions of the form,

$$\frac{p'(x,t)}{p} = X(x)\exp\left(2\pi \mathrm{i} f t\right) , \tag{2}$$

at a fixed frequency f leads to a general solution for axial dependence $X(x)$ comprising four characteristic waves: upstream-running pressure, $\hat{p}^-$; downstream-running pressure, $\hat{p}^+$; convected vorticity, $\hat{v}$; and convected entropy, $\hat{s}$ [7]. (If the axial flow is supersonic, both pressure waves are downstream-running at different speeds.)

To solve for the perturbation flow field throughout the turbine, the task is now to determine the four characteristic wave amplitudes in each control volume resulting from given boundary conditions. The annulus solutions must now couple to models for interactions between waves and blade rows.

2.2. Blade row modelling

After Kaji and Okazaki [11], assuming a narrow circumferential pitch implies that the flow within blade passages is one-dimensional. This treatment accounts for axial non-compactness, but neglects pitchwise non-compactness. For a perturbation of Eqn. (2) form, the solution comprises two pressure and entropy characteristic waves only (vorticity cannot exist in a one-dimensional flow).

In a blade row, mean flow quantities vary continuously from inlet to outlet conditions as the blades turn the flow. On physical grounds, acoustic perturbations propagating through a blade row must conserve mass, energy, and entropy. Therefore, $(\rho V_x)'$, T_0', and s' or equivalently p_0' are continuous as the mean flow varies, while the amplitudes of characteristic waves adjust to satisfy these requirements. Solving for four characteristic waves requires another boundary condition in addition to the three conservation laws — the Kutta condition, of no perturbation in outlet flow angle, $\alpha' = 0$, closes the system of equations. (If the exit flow were supersonic, a choking condition would apply instead.) The equations apply in the reference frame where a given blade row is stationary: absolute for stators, and relative for rotors.

The model encapsulates the resulting systems of equations in transfer matrices for each blade row, which yield the characteristic waves in the next control volume on multiplication with a vector of characteristic waves from the previous control volume. Full derivations of the transfer matrices for flat plate and cambered blade rows are given in Appendix B.

2.3. Entropy wave dispersion modelling

The model assumes one-dimensional flow within blade passages. In reality, there are mean flow gradients across the pitch and span, and the transit time of a fluid particle through the blade row varies for different locations over the row inlet. A plane entropy wave convected with the flow will not remain plane as it propagates through the blade row, and some of the entropy perturbation disperses to higher-order spatial modes. Leyko *et al.* [8] and Giusti *et al.* [15] independently proposed a method to account for this effect, which the present model includes. Tracking an array of streamlines through the blade row using three-dimensional CFD, convecting discrete entropy waves along each streamline, and then area-averaging at the exit of the blade row yields the remaining planar component. This forms an attenuation coefficient applied to reduce the amplitude of entropy waves exiting the blade row.

2.4. Solution by superposition method

With known transfer matrices for all blade rows, the model solves for the perturbations resulting from given machine inlet and outlet boundary conditions using a superposition method.

At the inlet boundary, the upstream-propagating pressure wave is unknown, as it depends on the response of the machine to the imposed disturbance. The outlet boundary condition is usually that there is no incident upstream-propagating wave. In this case, the solution procedure is,

1. Make an arbitrary guess, for the amplitude of the upstream-propagating characteristic wave at the inlet station;

2. By application of the successive transfer matrices, evaluate the waves at the exit of all subsequent blade rows and store this solution;
3. Make a second, distinct guess for the amplitude of the upstream-propagating characteristic wave at the inlet station;
4. Repeat step 2. with the new guess and store the solution;
5. Neither of these solutions will satisfy the desired outlet boundary condition, of no incident upstream-propagating pressure wave. Because the problem is linear, the solution is the linear combination of both guessed solutions which does satisfy this condition.

3. Time-marching computational method

Two-dimensional models are unable to capture the effects of spanwise non-uniformity on turbine acoustic impedance. The present work uses CFD to relax the assumptions of high hub-to-tip radius ratio and narrow blade pitch inherent in the analytical model. The approach is an extension of the CFD method used by Brind and Pullan [13] to three-dimensional cases.

For each geometry under consideration, a set of three unsteady simulations with different forcing about the same mean flow provide enough data to extract impedances to upstream- and downstream-running pressure and entropy waves. This approach, a version of the two-port 'black-box' technique proposed by Cremer [16], has the advantage of eliminating the need for non-reflecting or characteristic boundary conditions.

This section first describes the computational domain and specifies boundary conditions. Next, the section covers implementation details for the flow solver, discretisation, and calculation procedure. The section concludes with an outline of the post-processing steps required to extract acoustic impedances from sampled flow field data.

3.1. Domain and boundary conditions

Figure 4 shows the domain and boundary conditions for the CFD model of a multi-stage turbine on a meridional plane. The inlet boundary conditions are prescribed values of stagnation pressure and temperature, $p_{0,\mathrm{in}}(t)$ and $T_{0,\mathrm{in}}(t)$. The inlet flow is axial, as for flow exiting a gas turbine combustor. The inlet boundary conditions are functions of time, but spatially uniform. The outlet boundary condition is a prescribed static pressure on the inner annulus wall, $p_{\mathrm{out}}(t)$, together with the assumption of simple radial equilibrium to specify variation with radius. The boundary conditions are applied at a separation of one machine length away from the first vane and last rotor, of order one acoustic wavelength. The walls of the inlet and exit ducts are inviscid in order to prevent unrealistic boundary layer growth.

The domain is circumferentially periodic. In a conventional unsteady calculation, differing blade counts in each row of a multi-stage turbine require construction of a periodic sector with a circumferential extent covering several blade passages. Connecting adjacent rows with 'sliding planes', a circumferential interpolation procedure then matches the flow between grids in relative motion at each time step, allowing circumferential non-uniformity transfer through the machine.

The computational cost of multi-stage, periodic-sector calculations over multiple acoustic periods is large, of order 15 000 GPU hours to extract impedances for the case

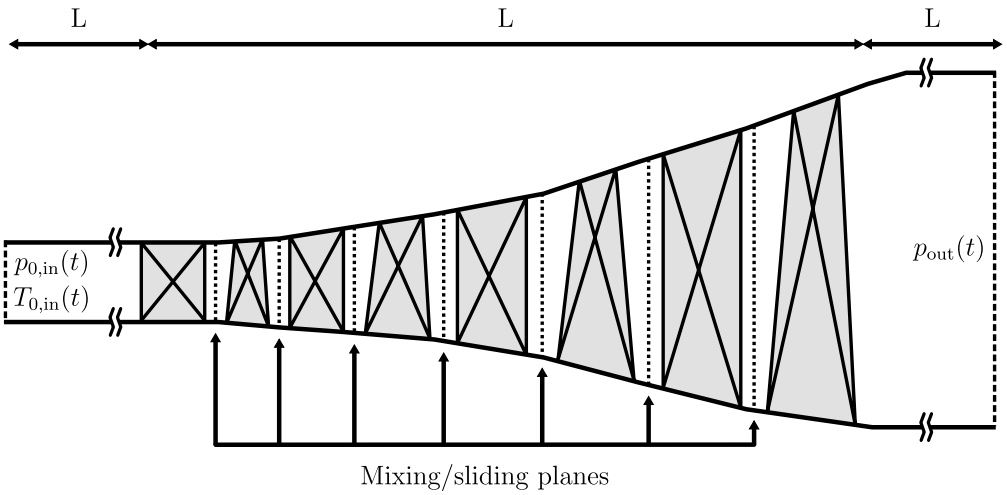

Figure 4: Domain and boundary conditions for multi-stage turbine simulations.

considered here. For thermoacoustic stability, planes waves are the primary subject of interest. This motivates a lower-fidelity model: running an unsteady calculation on single-passage meshes connected with 'mixing planes', which remove the need for a periodic sector by linking rows via circumferentially uniform (but radially non-uniform) boundary conditions.

Specifically, the current mixing plane treatment passes a pitchwise mass-averaged entropy and stagnation enthalpy to the downstream blade row, extrapolating variation in static pressure and flow angle from the interior; and passes the averaged fluxes of mass, momentum and energy upstream, extrapolating their circumferential variation from the interior while conserving mean levels. Mixing takes place separately at each radial location, allowing spanwise non-uniformity transfer between rows. Denton [17, 18] describes the approach in more detail. A single-passage model allows plane waves to propagate but neglects circumferential perturbations, and reduces computational cost by approximately one order of magnitude compared to the periodic sector model.

Section 4.2 presents results quantifying accuracy of the single passage approach, compared to a periodic sector.

3.2. Implementation details

All CFD simulations in this paper use the TURBOSTREAM 3 solver, a graphical processing unit accelerated, unsteady Reynolds-averaged Navier–Stokes (URANS) code developed by Brandvik and Pullan [19]. The code employs an algebraic mixing-length turbulence model, after Denton [18]. A wall function at a distance $\Delta y^+ \approx 30$ in wall units yields shear stress on solid boundaries, assuming fully turbulent boundary layers.

The acoustic boundary layer thickness is of order $\delta_{\mathrm{acoustic}} \sim \sqrt{\nu/\pi f}$, where ν is the kinematic viscosity. Relative to the turbine geometry, $\delta_{\mathrm{acoustic}}/c_x \sim 1.6 \times 10^{-3}$, suggesting that viscous effects will have a small influence on the acoustic field. The URANS equations with wall functions are sufficient to model the mean flow and essentially inviscid acoustic perturbations.

The spatial discretisation is second-order accurate finite volume, with at least 300 points per acoustic wavelength and 50 points per entropic wavelength. Multi-block structured O-H type computational meshes were generated using the commercial software Numeca AutoGrid5. The temporal discretisation is second-order accurate with an implicit dual time stepping scheme, with 72 time steps per blade passing.

Resolution studies verified that these spatial and temporal resolutions produce results independent of the discretisation level. At low reduced frequencies typical of combustion instability, the length and time scales of acoustic perturbations are much larger than those of blade rows. This means that a satisfactory resolution of the mean flow field also guarantees sufficient resolution of the acoustic field.

The black-box approach characterises the behaviour of a linear time-invariant system by observing responses to a set of linearly independent external inputs. In the present application, this means a set of simulations with the same turbine operating point, but different fluctuations about the time-averaged boundary conditions. Define a sum of sinusoids forcing function,

$$F = \sum_{m=1}^{M} \Delta \sin\left(2\pi m f_0 t\right) , \tag{3}$$

where f_0 is a fundamental frequency, M is a number of harmonics, and $\Delta = 0.1\%$ is a small amplitude parameter. Selected values of f_0 and M cover the reduced frequency range $\kappa \leq 0.1$, representative of combustion instability. Then, denoting the time-average using an overbar, one possible set of boundary condition perturbations is,

$$\text{I. Inlet isentropic forcing,} \quad \frac{p'_{0,\text{in}}}{\overline{p_{0,\text{in}}}} = F \ , \quad \frac{T'_{0,\text{in}}}{\overline{T_{0,\text{in}}}} = (1+F)^{\frac{\gamma-1}{\gamma}} - 1 \ ; \tag{4a}$$

$$\text{II. Inlet entropic forcing,} \quad \frac{p'_{0,\text{in}}}{\overline{p_{0,\text{in}}}} = 0 \ , \quad \frac{T'_{0,\text{in}}}{\overline{T_{0,\text{in}}}} = F \ ; \tag{4b}$$

$$\text{III. Outlet pressure forcing,} \quad \frac{p'_{\text{out}}}{\overline{p_{\text{out}}}} = F \ . \tag{4c}$$

The three unsteady simulations start from a converged steady solution and run to a periodic state over 40 fundamental forcing periods, before sampling of the flow field over another 12 periods.

3.3. Post-processing for reflection coefficients

This study characterises acoustic impedances in the form of reflection coefficients, which contain the same boundary condition information but are more convenient to work with because their magnitude is bounded by the unit interval.

During the time-marching simulations, flow field data are output for a series of streamwise locations in the inlet and exit ducts. A mixed-out averaging process makes the unsteady flow spatially uniform at each instant in time, while conserving mass, momentum and energy. Appendix A describes the averaging method in detail.

The multi-microphone method, after Poinsot et al. [20], separates upstream- and downstream-propagating pressure waves in the inlet and exit ducts. Using the Fourier-transformed static pressure $\check{p}(x, f)$ at sampling locations $x = x_1, x_2, \ldots, x_J$, the complex

characteristic wave amplitudes are the least-squares solution $\bar{\mathbf{x}}$ of,

$$\mathbf{A}\bar{\mathbf{x}} = \mathbf{b}\,, \quad \text{where,} \tag{5}$$

$$\bar{\mathbf{x}} = \begin{bmatrix} \hat{p}^+(f) \\ \hat{p}^-(f) \end{bmatrix}\,, \quad \mathbf{b} = \begin{bmatrix} \check{p}(x_1, f) \\ \check{p}(x_2, f) \\ \cdots \\ \check{p}(x_J, f) \end{bmatrix}\,, \tag{6}$$

$$\mathbf{A} = \begin{bmatrix} \exp(\mathrm{i}k^+x_1) & \exp(-\mathrm{i}k^-x_1) \\ \exp(\mathrm{i}k^+x_2) & \exp(-\mathrm{i}k^-x_2) \\ \cdots & \cdots \\ \exp(\mathrm{i}k^+x_J) & \exp(-\mathrm{i}k^-x_J) \end{bmatrix}\,, \quad k^+ = \frac{2\pi f}{a + V_x}\,, \quad k^- = \frac{2\pi f}{a - V_x}\,. \tag{7}$$

The entropy wave amplitude follows directly from the Fourier-transformed entropy perturbation $\check{s}(x, f)$. Phase shifting the pressure and entropy waves to reference planes at the leading edge of the first blade row, and trailing edge of the last blade row, ensures consistency with the analytical model.

Following the black-box method to solve for acoustic impedances, choosing state variables $\hat{p}^-_{\text{in}}$ and $\hat{p}^+_{\text{out}}$ and expressing them as a linear sum of contributions,

$$\underbrace{\hat{p}^-_{\text{in}}}_{\substack{\text{upstream-running} \\ \text{wave in inlet}}} = \underbrace{\hat{p}^+_{\text{in}}\mathcal{R}_{\hat{p}^+}}_{\text{reflection from turbine}} + \underbrace{\hat{p}^-_{\text{out}}\mathcal{T}_{\hat{p}^-}}_{\substack{\text{reflection from outlet,} \\ \text{transmitted back} \\ \text{through turbine}}} + \underbrace{\hat{s}_{\text{in}}\mathcal{R}_{\hat{s}}}_{\substack{\text{upstream-running} \\ \text{entropy noise}}}\,, \tag{8a}$$

$$\underbrace{\hat{p}^+_{\text{out}}}_{\substack{\text{downstream-running} \\ \text{wave in outlet}}} = \underbrace{\hat{p}^+_{\text{in}}\mathcal{T}_{\hat{p}^+}}_{\substack{\text{reflection from inlet,} \\ \text{transmitted back} \\ \text{through turbine}}} + \underbrace{\hat{p}^-_{\text{out}}\mathcal{R}_{\hat{p}^-}}_{\text{reflection from turbine}} + \underbrace{\hat{s}_{\text{in}}\mathcal{T}_{\hat{s}}}_{\substack{\text{downstream-running} \\ \text{entropy noise}}}\,, \tag{8b}$$

or in a more compact form,

$$\begin{bmatrix} \hat{p}^-_{\text{in}} \\ \hat{p}^+_{\text{out}} \end{bmatrix} = \begin{bmatrix} \mathcal{R}_{\hat{p}^+} & \mathcal{T}_{\hat{p}^-} & \mathcal{R}_{\hat{s}} \\ \mathcal{T}_{\hat{p}^+} & \mathcal{R}_{\hat{p}^-} & \mathcal{T}_{\hat{s}} \end{bmatrix} \begin{bmatrix} \hat{p}^+_{\text{in}} \\ \hat{p}^-_{\text{out}} \\ \hat{s}_{\text{in}} \end{bmatrix}\,. \tag{9}$$

The matrix on the right-hand side of Eqn. (9) is the 'scattering matrix' for the turbine, which contains reflection coefficients for all wave types. Assembling results from the independent simulations I, II, and III as specified in Eqns. (4) yields,

$$\begin{bmatrix} \hat{p}^-_{\text{in,I}} & \hat{p}^-_{\text{in,II}} & \hat{p}^-_{\text{in,III}} \\ \hat{p}^+_{\text{out,I}} & \hat{p}^+_{\text{out,II}} & \hat{p}^+_{\text{out,III}} \end{bmatrix} = \begin{bmatrix} \mathcal{R}_{\hat{p}^+} & \mathcal{T}_{\hat{p}^-} & \mathcal{R}_{\hat{s}} \\ \mathcal{T}_{\hat{p}^+} & \mathcal{R}_{\hat{p}^-} & \mathcal{T}_{\hat{s}} \end{bmatrix} \begin{bmatrix} \hat{p}^+_{\text{in,I}} & \hat{p}^+_{\text{in,II}} & \hat{p}^+_{\text{in,III}} \\ \hat{p}^-_{\text{out,I}} & \hat{p}^-_{\text{out,II}} & \hat{p}^-_{\text{out,III}} \\ \hat{s}_{\text{in,I}} & \hat{s}^+_{\text{in,II}} & \hat{s}^+_{\text{in,III}} \end{bmatrix}\,. \tag{10}$$

Solving the linear system in Eqn. (10) gives the scattering matrix.

4. Multi-stage turbine test case

This section considers a realistic multi-stage turbine of four stages, with three-dimensional blading, coolant flows, and leakage flows. Such a turbine is more complex than any of the idealised cases investigated previously in the literature, and stretches the assumptions of the analytical model. After a description of the details of the case, a comparison of acoustic impedance predictions against CFD validates the TAD model in a practical application. Then, results from the analytical model elucidate multi-stage effects on the acoustic impedance.

4.1. Case description

The design, illustrated in Fig. 4, is a proprietary geometry representative of large industrial gas turbines. The hub-to-tip radius ratio is approximately $HTR = 0.9$ for the first stage, reducing to $HTR = 0.6$ in the fourth stage. The blading is three-dimensional: stators use compound lean to reduce endwall loading and mitigate secondary flows; rotors twist to control the vortex distribution, and taper to reduce centrifugal loading.

The flow is subsonic, with typical relative Mach numbers $Ma \approx 0.2$ at row inlet and $Ma \approx 0.7$ at row exit. The Reynolds number based on first vane exit velocity and axial chord is of order $Re \approx 4 \times 10^6$. The turbine includes cooling, hub, and shroud leakage flows. The total flow of coolant is of order 25% inlet mass flow, the majority of which enters within the first stage. In CFD calculations, patches with prescribed injection fluxes of mass, momentum and energy model the integral effect of coolant flows without resolving detailed geometry. The analytical model injects all coolant flow for each row at the passage trailing edge.

With of order 1×10^6 grid points per blade passage, a mixing-plane computational domain requires 1×10^7 nodes. Modifying blade counts by up to 15% permits construction of a periodic 18° sector with 4×10^7 nodes in total. Despite modified blade counts, the computational cost of a periodic sector calculation is still one order of magnitude higher than a single-passage unsteady calculation. This is due to both an increased mesh size and smaller time step required to resolve blade row interactions.

4.2. Acoustic impedance results

Figure 5 compares predictions for acoustic impedance of the multi-stage turbine to an incident downstream-running pressure wave, between the TAD analytical method and both periodic sector and single-passage CFD models. Figures 5(a) and 5(b) show impedance magnitudes and phases.

The difference in impedance between sliding plane, periodic sector and mixing plane, single-passage simulations is small: a maximum of 4.7% in magnitude, and 0.03 rad in phase angle. This result implies that, when considering plane waves, a periodic sector model is unnecessary. Running a single-passage unsteady calculation, passing circumferentially averaged boundary conditions between blade rows, yields a saving in computation time of one order of magnitude. On this basis, Sections 5 and 6 investigate the effects of off-design operation and three-dimensional turbine design on acoustic impedance using single-passage CFD models.

CFD and analytical predictions of acoustic impedances are in close agreement. The root-mean-square discrepancy is 9% in magnitude, Fig. 5(a), and 0.06 rad in phase angle,

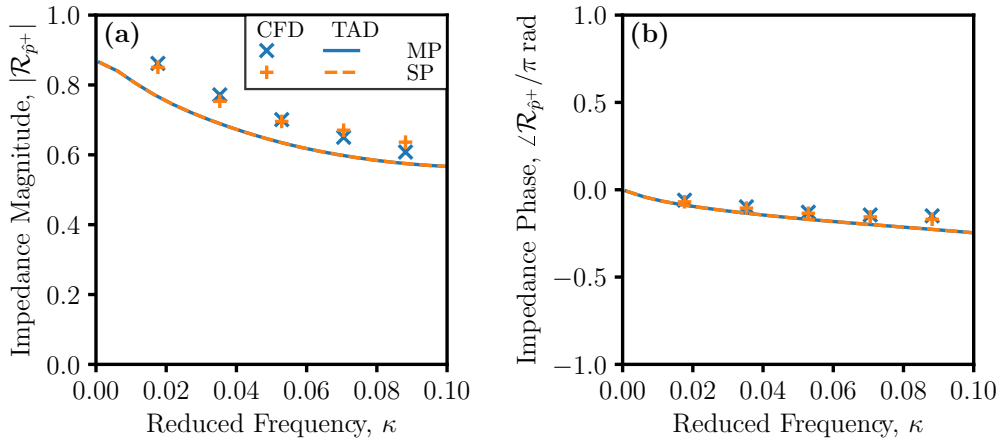

Figure 5: Acoustic impedance of multi-stage turbine to an incident downstream-running pressure wave, predicted by analytical model and CFD simulations: **(a)** magnitude, **(b)** phase. The CFD and analytical approaches agree to 9% in magnitude, and 0.18 rad in phase angle on average. Computations using mixing plane (MP) and sliding plane (SP) models agree to within 4.7% in magnitude, and 0.03 rad in phase.

Fig. 5(b). The maximum discrepancy is 11% impedance magnitude. This level of agreement is similar to that reported by Brind and Pullan [13] for a two-dimensional turbine stage, suggesting that the model remains applicable in realistic multi-stage geometries. The tendency of the analytical model to under-predict reflectivity is due to the assumptions of uniform mean flow in open annulus, and one-dimensional mean flow in blade passages. Such a simplified treatment can only approximate wave propagation through the true non-uniform flow.

Figure 6 compares analytical and CFD predictions for acoustic impedance of the multi-stage turbine to an incident convecting entropy wave. This paper defines the impedance as an entropy–acoustic transfer function between the entropy wave and resultant upstream-running entropy noise, suitably normalised as $\mathcal{R}_s = (\hat{p}^-/\hat{s})(c_v/p)$. As for incident pressure waves, periodic-sector and single-passage results are in good agreement, confirming applicability of the simpler CFD model.

The magnitude of the acoustic impedance is well-predicted by the analytical model, Fig. 6(a), with a root-mean-square discrepancy of 14% compared to the CFD data. The impedance phase in Fig. 6(b) matches to within 0.2 rad for $\kappa \leq 0.07$, but is in error by 0.5 rad at $\kappa = 0.09$.

Impedance phase shift is sensitive to the propagation time of the entropy wave as it convects through blade passages. Errors compound as incorrect transport through one blade row affects indirect noise contributions from subsequent blade rows. Non-compact effects are accentuated at the low inlet Mach number of this machine, $Ma = 0.14$, and high reduced frequency. Under these conditions, convection time scales are much slower than acoustic time scales, and accurate predictions require a higher-fidelity model — for example, the model of Emmanuelli et al. [21] convects entropy waves over streamtubes to model radial dispersion, and then discretises in the axial direction to capture non-compact effects.

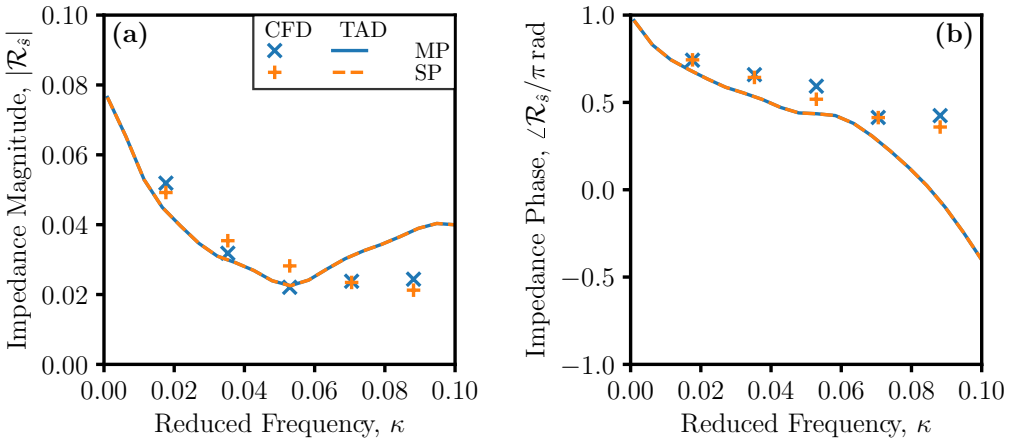

Figure 6: Acoustic impedance of multi-stage turbine to an incident downstream-running entropy wave, predicted by analytical model and CFD simulations: **(a)** magnitude, **(b)** phase. The CFD and analytical approaches agree to within 14% in magnitude, and the phases agree to within 0.2 rad for $\kappa \leq 0.07$.

4.3. Multi-stage effects

It is of interest to determine the contributions of each individual stage to the acoustic impedance of a multi-stage turbine. Suppose that the acoustic impedance is independent of the mean flow in the low-pressure turbine. From an analysis point of view, this permits a simpler model omitting the rear stages of the machine. From a design point of view, a combustion engineer can discount any influence from changes to the low-pressure turbine on thermoacoustic stability.

Applying the TAD analytical model to successively more stages of the turbine isolates the additional effect of each stage. From a steady CFD solution of the turbine, a series of partial models are generated, applying the exit boundary condition at a different location but maintaining the same mean flow in upstream stages. Figure 7 shows analytical predictions of reflection and transmission coefficients for partial models including one to four stages, compared to the four-stage CFD data.

From Figure 7(a), the downstream-running pressure wave reflection coefficient becomes independent of the number of stages once the model includes the first two stages. The same is true for entropy–acoustic reflection in Figure 7(b). Viewed from the combustor, the influence on acoustic impedance of each subsequent downstream turbine stage is decreasing. If the mean flow in the upstream stages stays constant, then modifications to the rear two stages will not affect impedances.

The transmission coefficient of pressure waves through the machine reduces as the number of stages increases, Figure 7(a), because the reflection from each additional row attenuates the transmitted wave. At $\kappa = 0.05$, the transmission coefficient of just one stage is a factor of eight greater than that of all four stages. In contrast, transmitted entropy noise increases with the number of stages for low frequencies, Figure 7(b). At such a low frequency, the entropy wave is only attenuated by dispersion effects through blade rows. The interaction with each successive stage adds more entropy noise that propagates downstream, the amplitude at $\kappa = 0.01$ increasing by a factor of three between

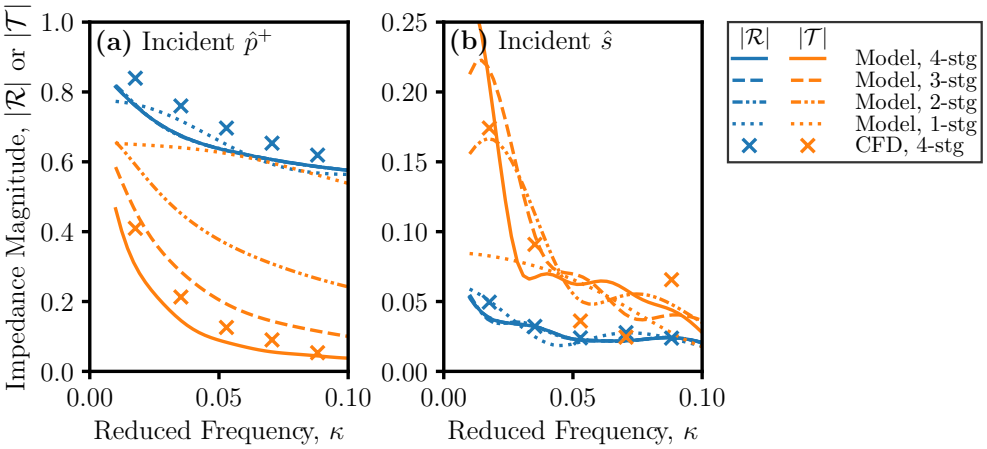

Figure 7: Effect of number of stages on acoustic impedances of multi-stage turbine predicted using TAD analytical model: **(a)** incident downstream-running pressure wave, **(b)** incident convective entropy wave. Reflection coefficients converge with two stages, while transmission coefficients require all four stages.

the one-stage and four-stage models. These results emphasise that a reduced number of stages is only sufficient to predict reflection coefficients, and prediction of transmission and downstream noise levels requires the full model.

Figure 8 illustrates the characteristic wave solutions within each row of the turbine obtained using TAD analytical models with two and four stages. As with Fig. 7, the mean flow is held constant, while the non-reflective acoustic boundary condition, of no upstream running wave, is applied at the exits of the second and fourth stage in turn.

The top row of plots, Fig 8(a), shows non-dimensional amplitudes, and the bottom row, Fig 8(b), shows phase angles. The horizontal axis of all plots is a row index through the machine. The four characteristic waves admitted by the linearised Euler equations are in columns: (i) downstream-running pressure, (ii) upstream-running pressure, (iii) convected vorticity, (iv) convected entropy. The results are for a low reduced frequency $\kappa = 0.02$. The closed circles indicate results from the full four-stage model, and the open circles for a model truncated after two stages.

Despite the exit boundary condition applying at different locations in the four- and two-stage models, from Figures 8(a.i) and 8(a.ii), the solutions for pressure waves in the front stages match to within $\pm 5\%$ of amplitude. There are negligible differences in the phases, 8(b). The upstream-running wave amplitude downstream of the second stage is $\hat{p}^- = 0.39$ in the full model, Figure 8(a.ii). Forcing this amplitude to zero as a boundary condition in the two-stage model has only a small impact on the upstream solution. It is hypothesised that internal reflections between the blade rows act to reduce sensitivity to boundary conditions.

5. Off-design operation

This section investigates changes in turbine acoustic impedance when the gas turbine operates away from its design point. Quantifying this effect is important because prac-

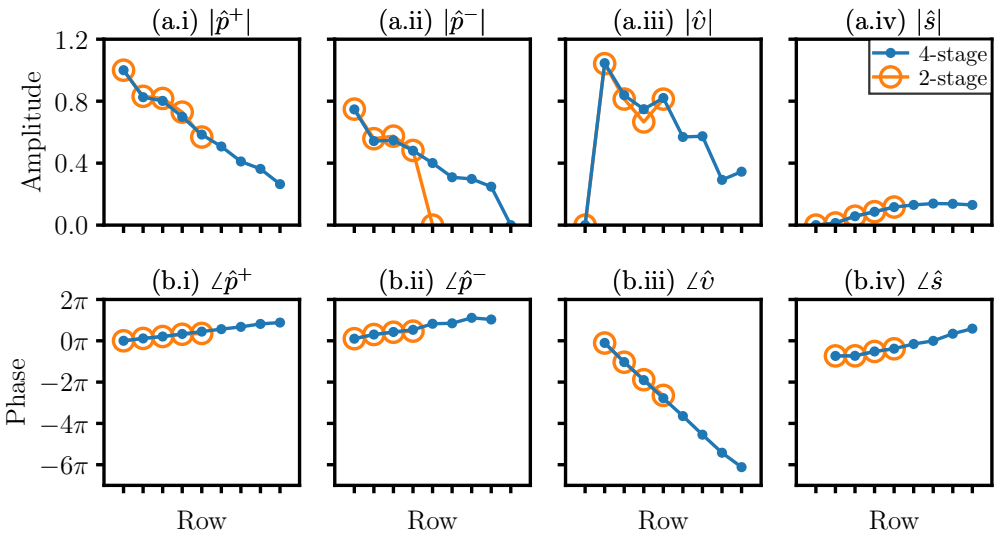

Figure 8: Propagation of characteristic waves through each row of multi-stage turbine, $\kappa = 0.02$, predicted by analytical model with two and four stages: rows **(a)** and **(b)** display magnitude and phase lag; columns **(i)** through **(iv)** show characteristic wave type. The solutions for the two- and four-stage models are identical in the front stages.

tical experience shows that the risk of thermoacoustic instability increases at part-load conditions [5].

There are two principle controls available to a gas turbine operator: fuel flow rate and compressor inlet guide vane setting. To model this operating range, the inlet boundary conditions of the multi-stage turbine from Section 4 are varied over a range of turbine inlet temperatures and mass flow rates defined by two normalised quantities,

$$\Theta = T_{01}/T_{01,\mathrm{d}}\,, \quad 0.6 \leq \Theta \leq 1\,, \tag{11}$$

and,

$$\Phi = \dot{m}_1/\dot{m}_{1\mathrm{d}}\,, \quad 0.7 \leq \Phi \leq 1\,, \tag{12}$$

where subscript d indicates the design point value.

The rotor shaft speed is held constant, as it would be in power generation applications, where the turbine drives a generator at a fixed electricity grid frequency. Coolant mass flow scales proportionally to inlet mass flow, while coolant temperatures remain the same at all operating points.

Single-passage unsteady CFD simulations and the TAD analytical model quantify how acoustic impedance varies over the entire turbine operation range.

5.1. Mean flow at off-design conditions

Any changes in acoustic behaviour will be due to changes in the mean flow field. Figure 9 uses data from time-averaged CFD simulations to indicate variations in mean flow over the operating points studied in this Section. The pressure–mass flow characteristic

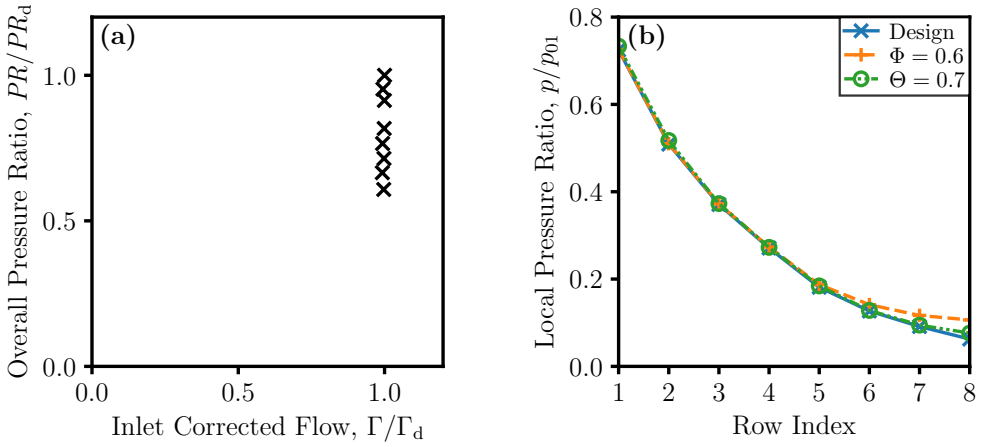

Figure 9: Effect of off-design operation on multi-stage turbine mean flow, CFD-predicted: **(a)** overall pressure ratio against inlet corrected flow characteristic, normalised by design point values; **(b)** static pressure downstream of each blade row, normalised by the inlet stagnation pressure, at different operating conditions. The overall characteristic is steep, and the flow field is invariant in the front two stages.

of Fig. 9(a) is in terms of overall pressure ratio, PR, against inlet corrected flow defined,

$$\Gamma = \dot{m}_1 \sqrt{T_{01}}/p_{01} \,. \tag{13}$$

Both quantities are normalised by their design point values. The slope of the characteristic is steep: over a 39% variation in pressure ratio the corrected flow varies by less than 1%.

The tendency for multi-stage turbines to operate at constant corrected flow is well known [22]. As row exit Mach number increases, the pressure ratio–mass flow characteristic becomes steeper, until the choking condition is reached and mass flow becomes independent of pressure ratio. Many rows in series magnify this effect, so that the multi-stage turbine behaves like a choked nozzle (with a constant value of corrected flow) even when Mach numbers in each row are subsonic.

Figure 9(b) shows static pressure downstream of each blade row, normalised by the inlet stagnation value, for the design operation condition and two off-design conditions. These are: low mass flow rate where $\Phi = \dot{m}_1/\dot{m}_{1,\mathrm{d}} = 0.6$, and low inlet temperature where $\Theta = T_{01}/T_{01,\mathrm{d}} = 0.7$. The static-to-stagnation pressure ratio across each row in the first two stages varies negligibly, and the traces only differ in the downstream two stages. The results of Section 4.3 show that the acoustic impedance of this multi-stage turbine is set by the upstream two stages. Given the same pressure ratios and inlet corrected flow in these stages, the Mach numbers and hence acoustic response of the turbine will be the same.

5.2. Mass flow rate reduction

Figures 10 and 11 display acoustic impedance results for a reduction in mass flow of up to 30% with $0.7 \leq \Phi \leq 1.0$, while maintaining the design turbine inlet temperature $\Theta = 1$. For incident downstream-running pressure waves in Fig. 10, both CFD and TAD

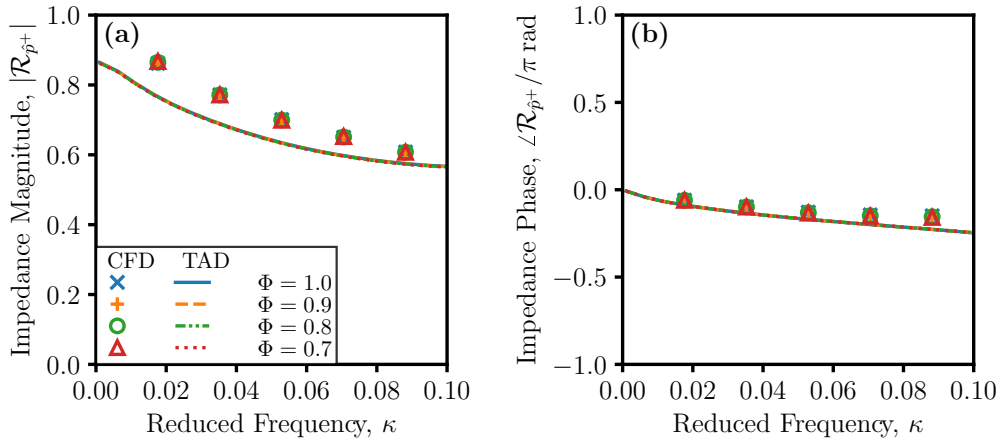

Figure 10: Effect of mass flow rate on acoustic impedance of multi-stage turbine to downstream-running pressure wave, predicted by TAD and CFD: **(a)** impedance magnitude, **(b)** impedance phase. The acoustic impedance is independent of mass flow rate.

predict the impedance to be independent of mass flow rate. This is consistent with the fixed corrected flow operation observed in Fig. 9(a); the mixed-out first vane exit Mach number for each of the four cases is constant to within 0.3% and hence variations in acoustic behaviour are negligible.

Now considering incident entropy waves in Fig. 11, the analytical model also predicts entropy–acoustic transfer functions to be independent of mass flow rate, while there is a spread in the CFD data of order 0.01 in magnitude and up to 0.5 rad in phase angle. There is no physical reason for the CFD data to show dependence on mass flow rate: when operating at fixed corrected flow, the *non-dimensional* acoustic field is always the same, as confirmed by the TAD results. The spread in CFD results is due to numerical effects, where discretisation and post-processing errors depend on the *dimensional* flow field, especially at higher frequencies.

5.3. Turbine inlet temperature reduction

Figure 12 shows the effect of turbine inlet temperature reduction by up to 30% with $0.7 \leq \Theta \leq 1.0$ at constant mass flow $\Phi = 1$, on the acoustic impedance to pressure waves. The dimensional value of the fundamental frequency is held constant, so that reduced frequencies for each CFD forcing harmonic increase with $\sqrt{\Theta}$.

Figure 12(a) displays small variations of up to 7% in impedance magnitude as the inlet temperature drops, reducing by of order 0.01 rad at $\Theta = 0.7$. The effect is not a numerical artifact, as it occurs in both TAD and CFD models. Although the inlet corrected flow remains constant, the dimensional coolant temperature is fixed for this study, so the temperature ratios for coolant injection will change, altering impedances. If coolant temperatures were appropriately scaled with the turbine entry temperature, results for different Θ would collapse, as with those for mass flow rate Φ in Fig. 10. The impedance phase in Fig. 12(b) is a weak function of turbine inlet temperature.

The analytical results in Fig. 13(a) show a consistent trend for reduction in the entropy–acoustic transfer function magnitude as turbine inlet temperature reduces, by

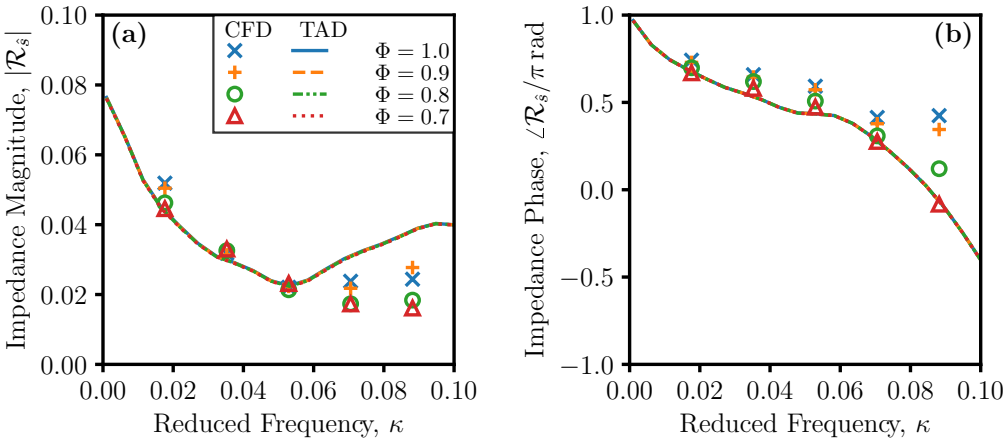

Figure 11: Effect of mass flow rate on acoustic impedance of multi-stage turbine to convecting entropy wave, predicted by TAD and CFD: **(a)** impedance magnitude, **(b)** impedance phase. The analytical model predicts the entropy–acoustic transfer function to be independent of mass flow rate, while the CFD results exhibit a spread at high frequencies attributable to numerical and post-processing artifacts.

up to 10%. This is because a rising coolant temperature ratio acts to reduce the first vane exit Mach number by up to 2% when $\Phi = 0.7$.

CFD results in Fig. 13 show a greater variation in impedance than the analytical model, of order 0.01, but without a consistent trend. As with Fig. 11, numerical effects are responsible. In particular, for the cases considered in this section, the mesh resolution and sampling probe locations are fixed, but the acoustic wavelength varies with turbine entry temperature. Hence, uncertainties in the CFD simulated and post-processed transfer functions are larger than the trend predicted by TAD. For other cases presented in this paper, the probe locations and forcing amplitude are optimised for fixed dimensional inlet boundary conditions, and uncertainties are at a minimum.

Overall, the results from this section confirm that the acoustic impedance of a multi-stage turbine may be assumed constant during off-design operation.

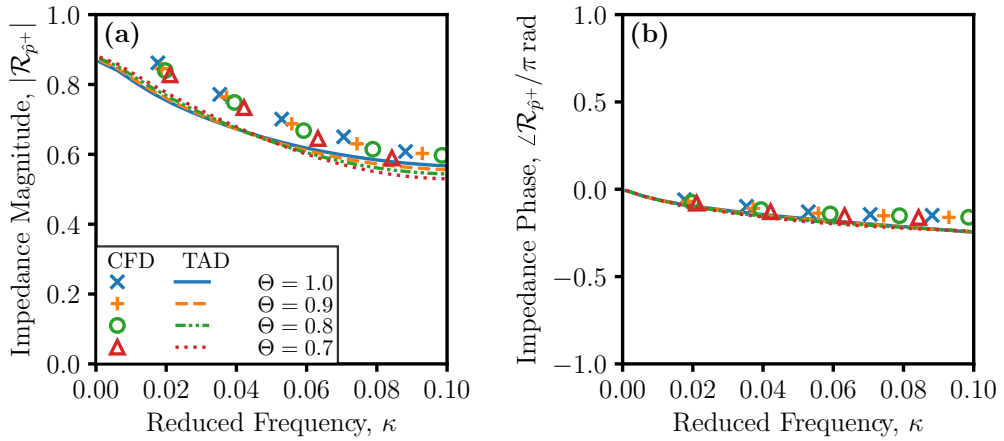

Figure 12: Effect of turbine inlet temperature on acoustic impedance of multi-stage turbine to downstream-running pressure wave, predicted by TAD and CFD: **(a)** impedance magnitude, **(b)** impedance phase. Impedance varies by up to 7% at low turbine inlet temperatures, due to an increase in coolant temperature ratio.

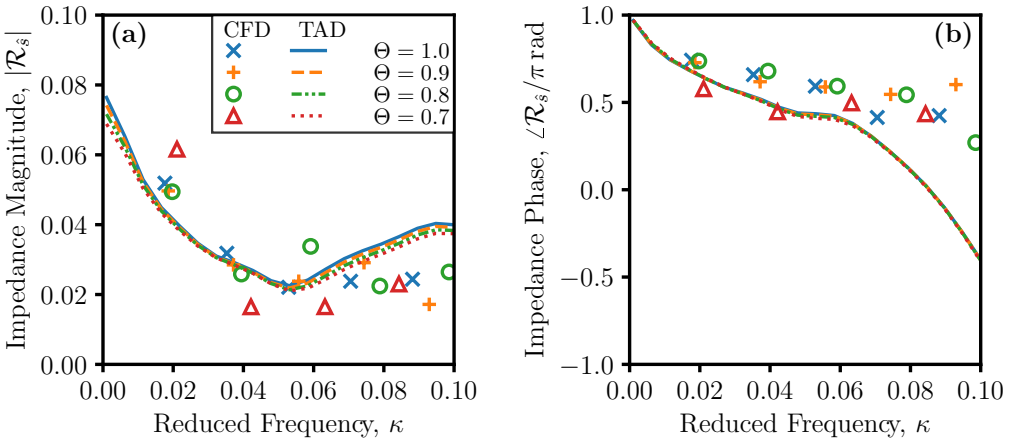

Figure 13: Effect of turbine inlet temperature on acoustic impedance of multi-stage turbine to convecting entropy wave, predicted by analytical model and CFD: **(a)** impedance magnitude, **(b)** impedance phase. TAD predicts a weak sensitivity, while CFD results show variations of order 0.01 in entropy–acoustic transfer function.

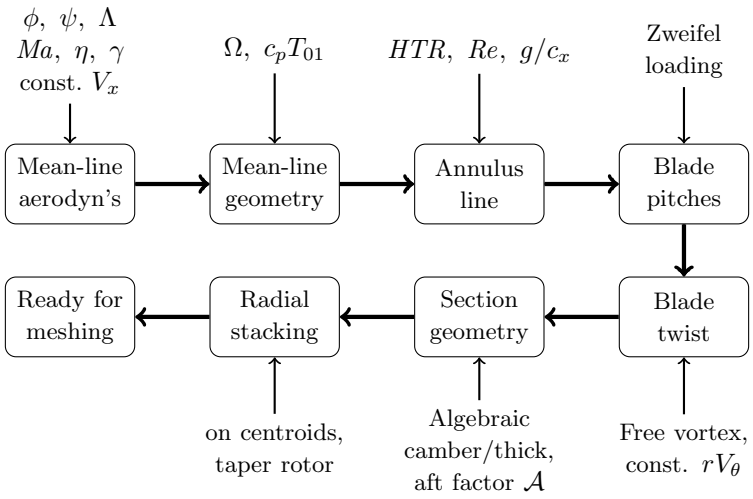

Figure 14: Flowchart for turbine stage geometry generation procedure.

6. Three-dimensional turbine design

This section quantifies the effect of geometry changes on the acoustic impedance of three-dimensional turbine stages. Brind and Pullan [13] investigated the influence of mean-line aerodynamic design on acoustic impedance, changing one-dimensional parameters such as flow coefficient and stage loading coefficient. The present work considers more detailed design changes to a three-dimensional turbine stage, while maintaining a constant one-dimensional operating point.

A parametric geometry generation system yields families of similar turbine stage designs, independently varying: hub-to-tip radius ratio, chordwise loading distribution, and stator–rotor axial gap; while holding annulus-averaged flow at the same values in all cases. Single-passage unsteady CFD simulations and the analytical TAD model predict the resultant effects on acoustic impedance.

6.1. Geometry generation algorithm

To create sets of comparable turbine geometries requires a consistent design method proceeding from first principles. The method uses standard turbomachinery aerodynamics parameters as defined by Dixon and Hall [23]. Figure 14 illustrates the input data required at each step in the process, described below:

- Input the mean-line velocity triangle design parameters: flow coefficient, stage loading coefficient, degree of reaction, vane exit Mach number, estimated polytropic efficiency, axial velocity ratio, and ratio of specific heats;
- Use the Euler work equation and perfect gas compressible flow relations to convert these *aerodynamic* non-dimensional groups into a set of *geometric* non-dimensional parameters characterising the mean-line: flow angles, axial velocity density ratios, and a normalised blade speed $U/\sqrt{c_pT_{01}}$;

- Choose an arbitrary inlet enthalpy, c_pT_{01}, and shaft angular velocity, Ω, to calculate a mean radius from the normalised blade speed;
- Input a value of hub-to-tip radius ratio, $HTR = r_{\text{hub}}/r_{\text{tip}}$, and set the radial spans using the calculated mean radius and axial velocity density ratios;
- Input a vane exit Reynolds number, Re_2, to fix the chord length, assuming the stator and rotor chords are equal;
- Input the stator–rotor gap, g/c_x, and the annulus line of the stage is fully defined;
- Input a Zweifel loading coefficient, Z, to set blade pitches;
- Specify flow angles away from mid-span using a free-vortex swirl distribution, with constant rV_θ;
- Input an aft-loading factor, $\mathcal{A}$, and evaluate a cubic camber line where the metal angle χ is a function of axial chord fraction x/c_x,

$$\tan\chi\left(\tfrac{x}{c_x}\right) = (\tan\chi_2 - \tan\chi_1)\left[\mathcal{A}\left(\tfrac{x}{c_x}\right)^2 + (1-\mathcal{A})\tfrac{x}{c_x}\right] + \tan\chi_1\,, \quad 0 \le \tfrac{x}{c_x} \le 1\,; \tag{14}$$

- Apply a simple algebraic thickness distribution from Denton [17] symmetrically about the camber line to create vane and blade sections at each radial location;
- Stack the sections radially on their centroids;
- Taper the rotor in axial and circumferential directions to a representative area ratio of 1/2;
- Output annulus line and blade section coordinates for meshing.

Table 1 lists mean-line and three-dimensional design parameters for the turbine stages presented in this section. Although the resulting designs are not optimal, and would benefit from manual changes to the blade sections and radial vortex distributions, their performance is adequate, with a CFD-predicted polytropic efficiency within one percentage point of the target value $\eta = 0.95$. More importantly, the designs are comparable to each other, and vary only one parameter at a time. Figure 15 shows the blade shapes and well-behaved flow pattern at mid-span in the datum turbine stage using CFD predictions of relative Mach number.

6.2. Hub-to-tip radius ratio

The analytical model assumes high hub-to-tip radius ratio, to make the governing equations two-dimensional; only CFD can capture the effect of spanwise non-uniformity on acoustic impedance. Section 4.2 shows that the analytical model nevertheless yields an adequate prediction for a three-dimensional turbine with a hub-to-tip radius ratio of $HTR = 0.9$ in the first stage.

This section will further show that the TAD analytical model is accurate down to low hub-to-tip radius ratios, using a set of turbine stages with $0.6 \le HTR \le 0.9$ generated using the procedure of Section 6.1. As radial span increases, mass flow rate also increases,

Table 1: Input data for turbine geometry generation, with datum values.

Mean-line parameters	Inlet flow angle,	$\alpha_1 = 0°$
	Flow coefficient,	$\phi = 0.6$
	Stage loading coefficient,	$\psi = 1.6$
	Degree of reaction,	$\Lambda = 0.5$
	Constant axial velocity	
	Vane exit Mach number,	$Ma_2 = 0.75$
	Vane exit Reynolds number,	$Re_2 = 4 \times 10^6$
	Ratio of specific heats,	$\gamma = 1.33$
	Estimated polytropic efficiency,	$\eta = 0.95$
	Zweifel coefficient,	$Z = 0.85$
Three-dimensional parameters	Hub-to-tip radius ratio,	$HTR = 0.9$
	Aft-loading factor,	$\mathcal{A} = 0.0$
	Stator–rotor axial gap,	$g/c_x = 1.0$

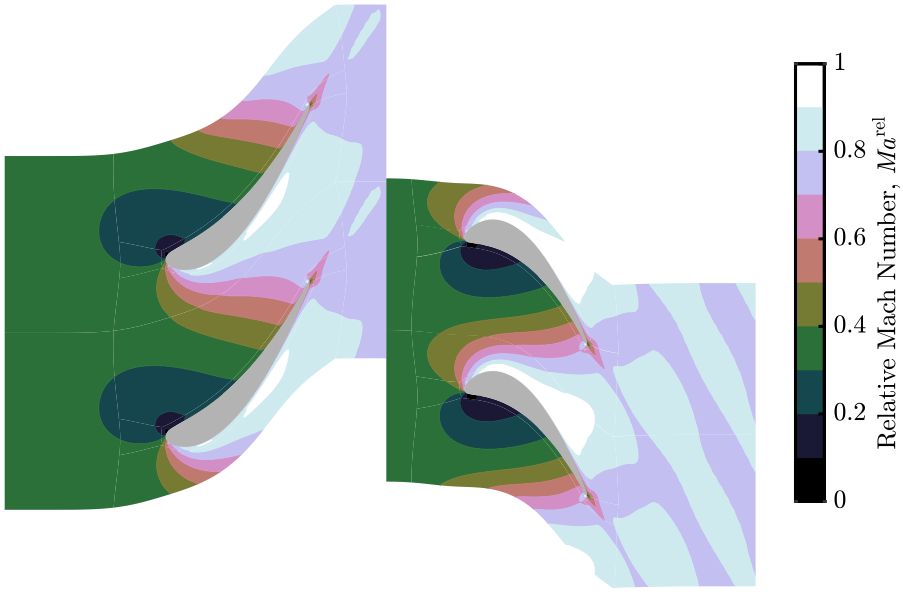

Figure 15: Contours of relative Mach number at mid-span for the datum generated turbine geometry, predicted by CFD. The flow field is subsonic and well-behaved.

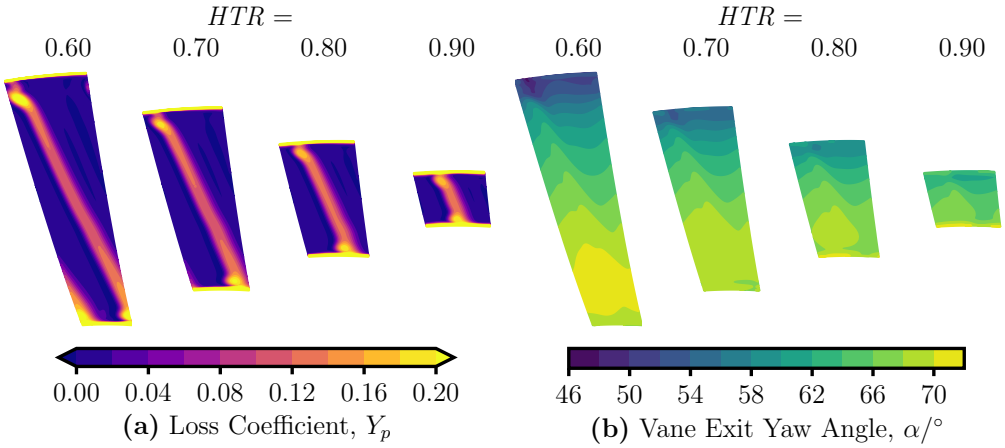

Figure 16: Vane exit flow fields, predicted by CFD, for turbine stage designs at varying hub-to-tip radius ratio: **(a)** Contours of stagnation pressure loss coefficient, referenced to isentropic exit dynamic head, **(b)** contours of yaw angle. The flow is three-dimensional, with spanwise non-uniformity.

while the annulus-averaged flow coefficient, stage loading coefficient, degree of reaction, and vane exit Mach number remain constant to within ±0.9%. If spanwise non-uniformity has no influence, these geometries would all have similar acoustic impedances, with any differences due to small changes in one-dimensional flow parameters.

Figure 16 illustrates vane exit flow fields in the family of turbine stages with different hub-to-tip ratios. Contours of stagnation pressure loss coefficient in Fig. 16(a) show secondary loss cores and boundary layers at the endwalls, with lower loss at mid-span. Fig. 16(b) shows that swirl reduces towards the casing, as expected from a free-vortex distribution. This is necessary to satisfy radial equilibrium while maintaining a constant axial velocity.

Figure 17 shows results for the acoustic impedance of this family of turbine stages to a downstream-running pressure wave, comparing between TAD and CFD. Despite radial variations in flow angle of up to 25° (Fig. 16(b)), violating the two-dimensional assumption of the analytical model, Fig. 17(a) shows good agreement between TAD and CFD for all hub-to-tip ratios, with a root-mean-square discrepancy of 5% in impedance magnitude over all cases. At $\kappa = 0.09$, CFD predicts a drop in impedance of 13% as the hub-to-tip ratio reduces from $HTR = 0.9$ to $HTR = 0.6$, and the analytical model a drop of 11%. Because both methods capture this effect, the cause must be the small changes in one-dimensional mean flow between designs. The acoustic impedance phase, in Fig. 17(b), is insensitive to hub-to-tip ratio according to both model and CFD predictions.

Considering the entropy–acoustic transfer function in Fig. 18, the results are similar to those observed for incident pressure waves. At constant mean-line design, the influence of hub-to-tip ratio and associated radial non-uniformity is weak. Notwithstanding a systematic over-prediction by TAD of 30% in magnitude at $\kappa = 0.07$, both CFD and analytical model agree that the entropy–acoustic transfer function varies by less than ±10% as hub-to-tip ratio is varied.

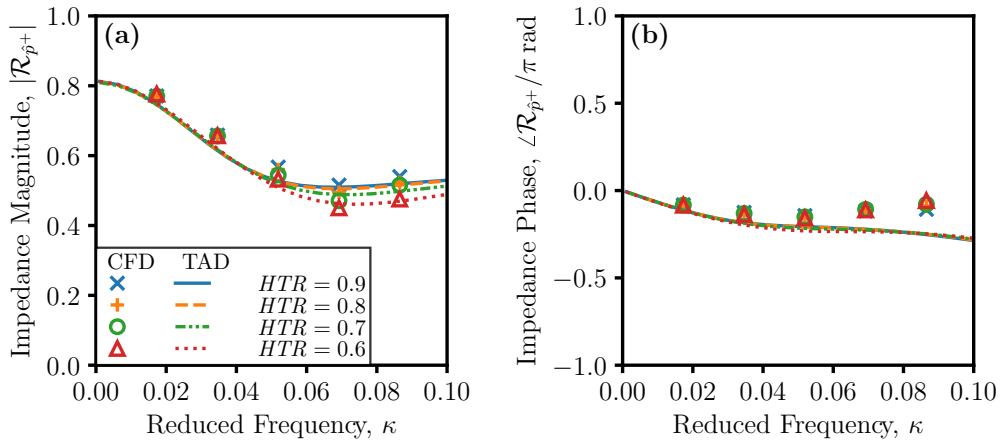

Figure 17: Effect of hub-to-tip ratio on acoustic impedance of a turbine stage to downstream-running pressure wave, predicted by TAD analytical model and CFD: **(a)** impedance magnitude **(b)** impedance phase. As hub-to-tip ratio reduces, impedance magnitude reduces by up to 15%, a trend captured by both analytical model and CFD. Impedance phase is insensitive to hub-to-tip ratio.

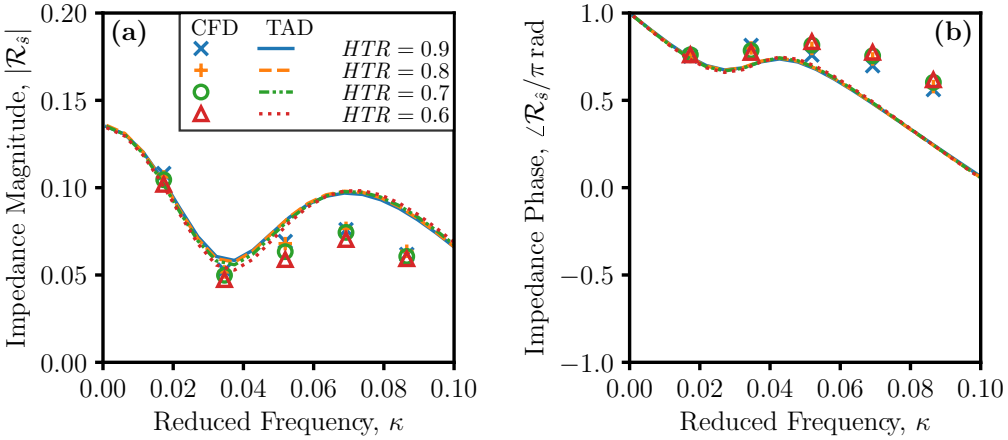

Figure 18: Effect of hub-to-tip ratio on acoustic impedance of a turbine stage to convecting entropy wave, predicted by TAD analytical model and CFD: **(a)** impedance magnitude **(b)** impedance phase. Both magnitude and phase of the entropy–acoustic transfer function are independent of hub-to-tip-ratio.

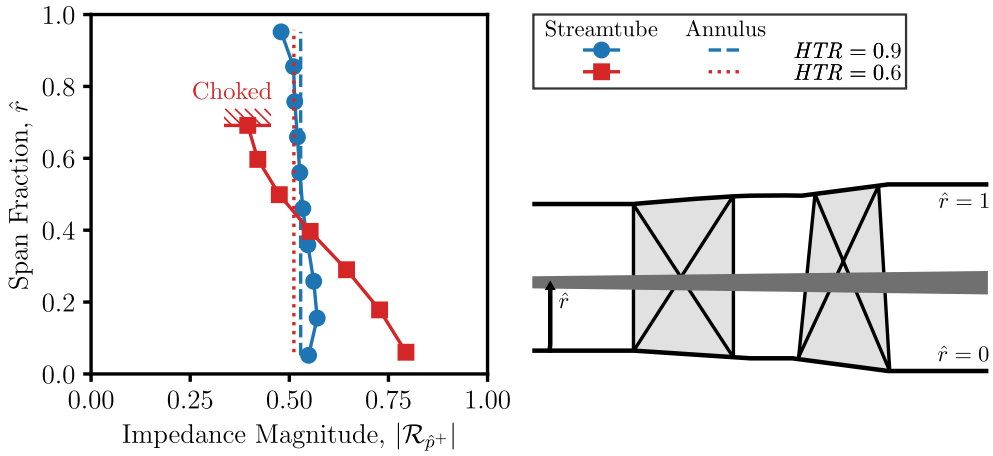

Figure 19: Radial variations in acoustic impedance of streamtubes through a turbine stage at $\kappa = 0.05$, predicted by analytical model. At $HTR = 0.9$, the impedance of all streamtubes varies by $\pm 9\%$; at $HTR = 0.6$, the hub streamtube impedance is 55% over the mean value, while the impedance reduces towards the casing where the streamtubes choke for $\hat{r} > 0.75$. The annulus-averaged impedances in the two cases differ by 3%.

Splitting the annulus into axisymmetric streamtubes allows examination of the local impedance at each spanwise location. The mean flow at inlet and exit planes of the stage is separated radially into bands each comprising 10% of the total mass flow, and input to the analytical model. Figure 19 compares the predicted acoustic impedances of each streamtube with the impedance for the entire annulus.

At high hub-to-tip ratio, $HTR = 0.9$, the acoustic impedance of each streamtube is within $\pm 9\%$ of the annulus-averaged value, with impedance trending down as radius increases. Although the flow is three-dimensional, the effect of this degree of radial non-uniformity on acoustic impedance is weak.

At low hub-to-tip radius ratio, $HTR = 0.6$, the degree of radial non-uniformity is greater, accentuating the trend of reducing impedance with radius. The local acoustic impedance is 55% over the annulus-average at the hub, because flow turning through the rotor is greatest at this location. Rotor turning decreases for streamtubes at higher radii, presenting less of a blockage for incident acoustic waves. Near the tip, the rotor exit relative Mach number exceeds unity, and the analytical model is not applicable.

Figure 19 shows why the two-dimensional analytical model gives accurate predictions of acoustic impedance, even for low hub-to-tip radius ratios where three-dimensional effects might be anticipated. Radial non-uniformity does have a first-order influence on the local acoustic impedance. However, variations in impedance due to variations in mean flow are approximately linear, such that increased impedance at the hub and reduced impedance at the tip balance out. The acoustic impedance of the annulus, averaged over all streamtubes, is close to the acoustic impedance given by a radially averaged flow.

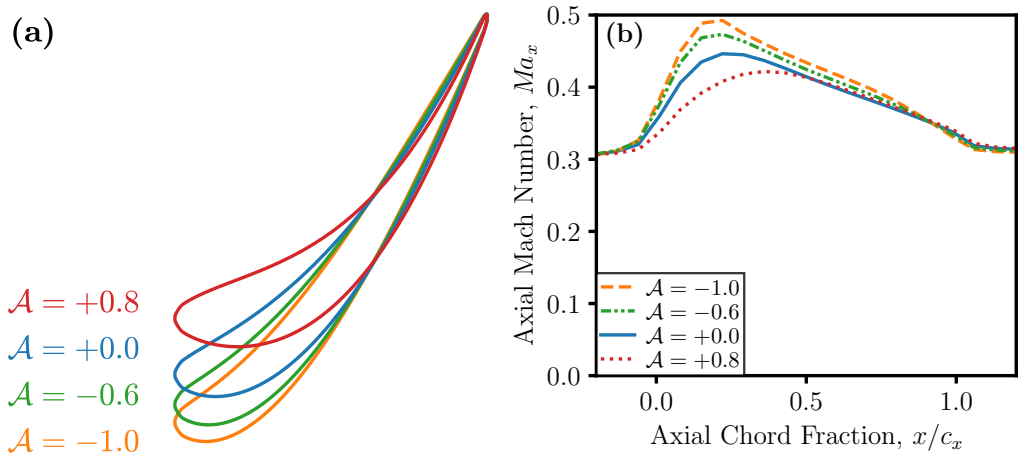

Figure 20: Variation in camber line for a turbine vane using aft-loading factor $\mathcal{A}$: **(a)** section geometry, **(b)** streamwise distribution of area-averaged axial Mach number. High values of $\mathcal{A}$ yield curved camber lines, with turning delayed towards the rear of the passage; low values of $\mathcal{A}$ approach flat plate geometry. As $\mathcal{A}$ increases, axial Mach number rises within the passage, while remaining constant outside.

6.3. Camber

The shape of an aerofoil camber line controls the chordwise loading distribution, that is, the fraction of total turning performed up to a given point in the blade passage. A 'front-loaded' blade row does most turning around the leading edge, while an 'aft-loaded' blade row delays turning until the flow is well inside the passage. With fixed inlet and exit flow angles, a designer has freedom to vary the camber line to minimise attached boundary layer [24] and secondary flow [25] losses. This section will show that front-loading also increases the row acoustic impedance at non-compact frequencies.

Modifying the aft-loading factor $-1 \leq \mathcal{A} \leq 0.8$ in the definition of the camber line, Eqn. (14), generates a family of turbine stage designs with the same mean-line operating point, but different chordwise loading distributions. Aft-loaded blades have $\mathcal{A} > 0$; front-loaded blades have $\mathcal{A} < 0$. Recambering applies to both the stator and rotor with the same value of $\mathcal{A}$. To correct for changes in deviation due to modified aerofoil shape requires an additional iterative step to the geometry generation described in Section 6.1: restaggering the stator and rotor (through a solid-body rotation) until the annulus-averaged flow angles match those of the datum $\mathcal{A} = 0$ case. The mean-line flow parameters of the final designs match to within $\pm 1\%$.

Figure 20 shows the effect of varying aft-loading factor on aerofoil geometry, in Fig. 20(a), and on chordwise distribution of passage-averaged Mach number in Fig. 20(b). At low values of $\mathcal{A}$, the vane section approaches a flat shape with a straight camber line, while high values of $\mathcal{A}$ produce more curvature. Performing turning earlier accelerates the flow, so that the axial Mach number throughout the passage increases monotonically throughout the passage as $\mathcal{A}$ reduces, while Mach numbers outside the passage remain constant.

In the compact limit, a turbine becomes a discontinuity in mean flow with respect to a much larger acoustic wavelength, and acoustic impedance is independent of geometry.

Therefore, variations in the camber line can only affect impedance at non-compact frequencies. CFD results for impedances subject to incident downstream-running pressure waves in Figure 21(a) confirm this reasoning. For $\kappa \leq 0.03$, the impedance magnitude varies by less than $\pm 2\%$ when changing the aft-loading factor over $-1 \leq \mathcal{A} \leq 0.8$. At higher frequencies, however, aft-loading reduces impedance magnitude by up to 16% compared to the datum quadratic camber line, and front-loading increases impedance magnitude by up to 51%. Aft-loading also reduces the impedance phase, Fig. 21(b), by a maximum of 0.23 rad at $\kappa = 0.07$.

Figure 22 illustrates the influence of aft-loading on entropy–acoustic transfer functions for the family of recambered turbine stages. From CFD results in Fig. 22(a), there is no effect at low reduced frequencies, while the impedance magnitude increase for front-loaded blades for $\kappa \geq 0.04$. The maximum entropy acoustic transfer function occurs for $\mathcal{A} = -1$ at $\kappa = 0.05$, 43% over the datum quadratic camber line. Aft-loading with $\mathcal{A} < 0$ reduces the impedance by no more than 5%. The impedance phase results in Fig. 22(b) display a reduction as the aft-loading factor $\mathcal{A}$ increases, of order 0.15 rad for frequencies $\kappa \geq 0.03$.

The TAD model accommodates changes in camber line by altering the chordwise distribution of flow angle for each of the coupled semi-actuator disks according to Eqn. (14). Usually, the analytical method produces correct trends in impedance magnitude and phase, but under-predicts the size of the aft-loading effect in Fig. 21(a), and incorrectly predicts an increase in impedance for aft-loaded turbines at high reduced frequency in Fig. 22(a). With front- or aft-biased chordwise loading distributions, the maximum local loading is higher and pitchwise flow field variations are greater. However, the model assumes one-dimensional flow in blade passages, and any deviations from this simplification contribute to increased errors.

A front-loaded blade accelerates the flow further upstream than an aft-loaded blade, meaning that Mach numbers are higher throughout a front-loaded blade passage. The increase of acoustic impedance for front-loaded blades is then consistent with the known result that higher vane exit Mach number leads to higher impedance [11, 13].

The physical mechanism responsible is interference between waves reflected from different parts of the camber line. Gradients in mean flow along the chord contribute continuously to the total reflected wave. The discrete analog of this situation in the TAD model is a sum of waves reflected from both leading and trailing edges, and between each intermediate camber line element. In the compact limit, the phase delay for waves propagating over the blade chord is negligible, and independent of the flow within the passage. At higher reduced frequencies, the phase delay is a function of the chordwise axial Mach number distribution. For the turbine considered here, front-loading changes the phase delay such that interference is more constructive, and acoustic impedance increases compared to the datum.

Additional calculations using the TAD model confirm that the qualitative trend of increased impedance with front-loaded camber lines replicates across the entire mean-line design space considered by Brind and Pullan [13]. That is, the interference effect described above is not a strong function of the specific turbine velocity triangles.

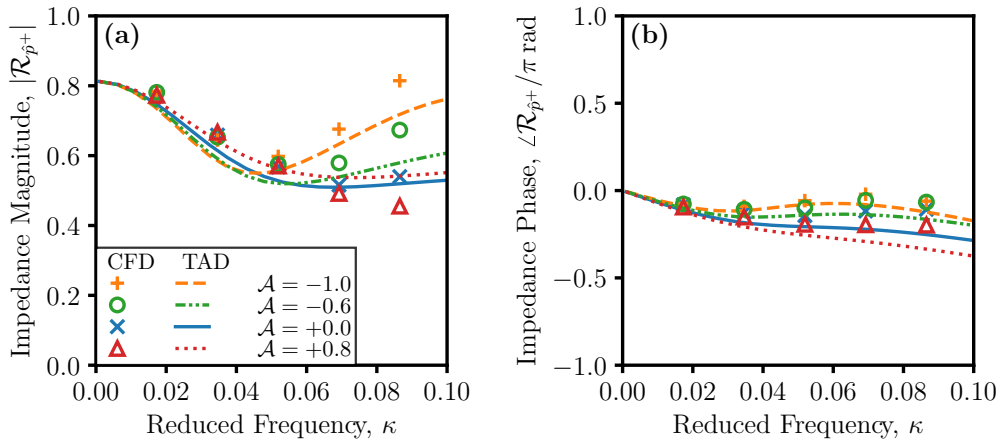

Figure 21: Effect of chordwise loading distribution on acoustic impedance of a turbine stage to downstream-running pressure wave, predicted by analytical model and CFD: **(a)** impedance magnitude , **(b)** impedance phase. Compared to the datum quadratic camber line, at $\kappa = 0.09$, aft-loading reduces impedance by 16%, and front-loading increases impedance by 51%.

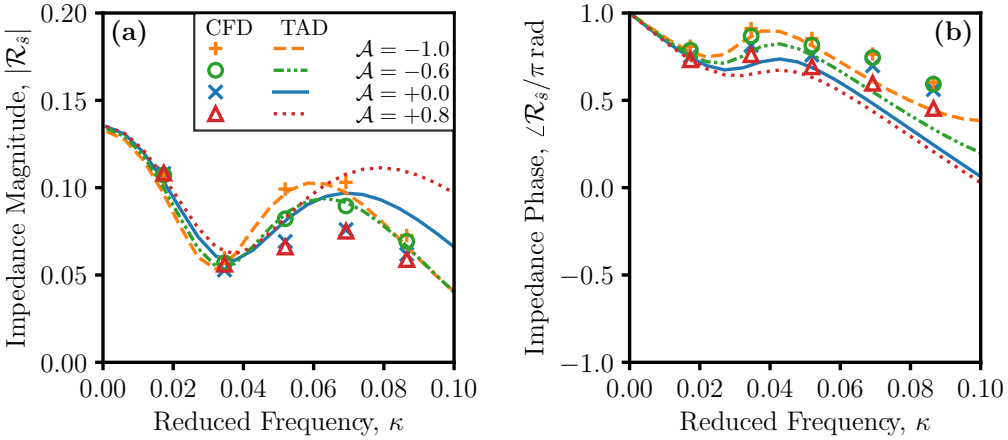

Figure 22: Effect of chordwise loading distribution on acoustic impedance of a turbine stage to convecting entropy wave, predicted by analytical model and CFD: **(a)** impedance magnitude , **(b)** impedance phase. Compared to a datum quadratic camber line, front-loading increases impedance by up to 43%.

6.4. Stator–rotor gap

A mean-line analysis cannot determine the optimum axial spacing between stator and rotor rows. The designer will trade off increased endwall loss and overall length at large gaps, with increased unsteady fatigue loading at small gaps. In addition, this section shows that acoustic impedance is a function of axial spacing, even at low reduced frequencies close to the compact limit of order $\kappa \approx 0.02$.

The annulus lines of the present turbine stages diverge within blade rows, and are parallel outside of blade rows (neglecting fillets to smooth sharp corners). Therefore, simply translating the rotor row in the axial direction generates stages with different stator–rotor gaps in the range $0.5 \leq g/c_x \leq 1.5$. Figure 23 shows meridional views of this set of turbines. The mean-line flow parameters are constant to within $\pm 0.3\%$.

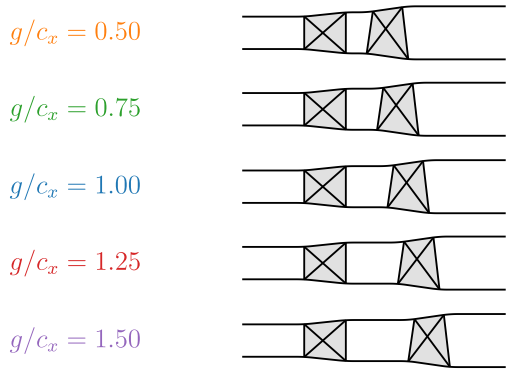

Figure 23: Annulus lines of turbine stages with varying stator–rotor axial gaps g/c_x.

Figure 24 shows acoustic impedance results for a downstream-running pressure wave incident on turbine stages with different stator–rotor axial gaps. All impedances converge to the same value of $\left|\mathcal{R}_{\hat{p}^+}\right| = 0.81$ in the compact limit as $\kappa \to 0$, Fig. 24(a), but impedance reduces as axial gap increases for reduced frequencies $0.02 \leq \kappa \leq 0.06$. CFD predicts a drop in impedance of 11% at $\kappa = 0.035$ as g/c_x increases from 0.5 to 1.5. The analytical model quantitatively matches this trend, predicting a corresponding drop of 12%. There is a crossover region, where the impedance magnitude is insensitive to axial spacing, around $0.055 \leq \kappa \leq 0.07$, above which the trend reverses and reflection coefficient increases with axial spacing. Impedance phase results in Fig. 24(b) exhibit sensitivity to axial gap in the same region where the impedance magnitude is insensitive. Increasing gap increases the impedance phase by of order 0.04 rad.

Figure 25 shows impedance results for a convecting entropy wave incident on the turbine stages with varying axial gaps. The effect of axial gap on impedance magnitude, Fig. 25(a), varies depending on the frequency under consideration: a negative trend at low and high frequency, and a positive trend between two cross-over points $0.035 \leq \kappa \leq 0.08$. The maximum increase in entropy impedance is a factor of two at $\kappa \leq 0.05$. Impedance phase, Fig. 25(b), is most sensitive around the cross-over points, and least sensitive at $\kappa = 0.05$ where the magnitude effect is largest. The behaviour in Fig. 25 is qualitatively consistent with Fig. 24.

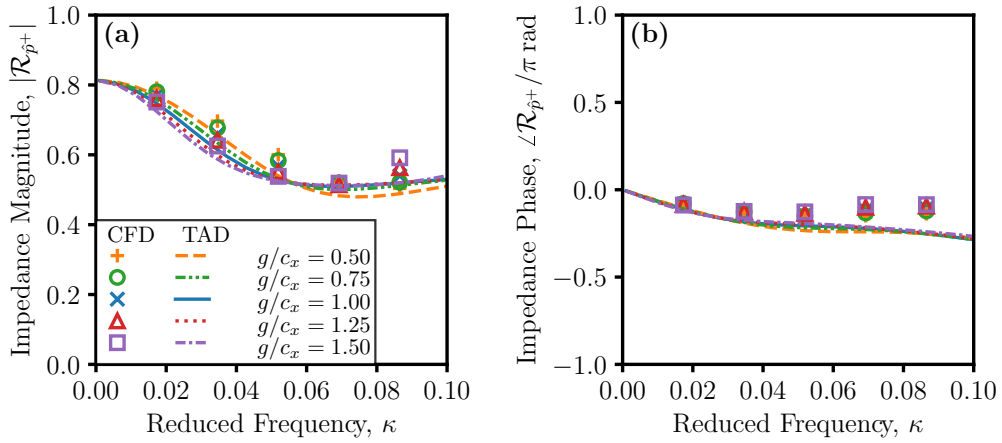

Figure 24: Effect of stator–rotor axial gap size on acoustic impedance of a turbine stage to downstream-running pressure wave, predicted by analytical model and CFD: **(a)** impedance magnitude, **(b)** impedance phase. The impedance magnitude reduces by up to 11% with increasing axial gap for $0.01 \leq \kappa \leq 0.06$.

As the problem is linear, the response of a turbine stage to an incident downstream-running pressure wave decomposes into a superposition of two stator-only cases, illustrated in Fig. 26. These are: (i) the incident downstream-running pressure wave, and (ii) an incident upstream-running pressure wave originating from reflection at the rotor. Case (ii) is the subtraction of case (i) from the full stage solution. Figure 26 also shows the inlet upstream-running wave present in each case, together with the total impedance, as phasors. The plot shows results for all axial gaps at two reduced frequencies, $\kappa = 0.03$ and $\kappa = 0.06$.

The stator contribution makes up most of the total impedance, and is independent of axial gap (Fig. 26, the lone pink symbols). The rotor contribution, however, is a function of axial gap, because it depends on the phase shift of waves crossing the gap (Fig. 26, teal symbols with lines attached). At $\kappa = 0.03$, the relative phase of rotor and stator contributions is such that the magnitude of the complex sum reduces as gap increases (Fig. 26, radial line inwards from grey cross). At $\kappa = 0.06$ the variation in rotor contribution lies perpendicular to the stator contribution phasor, such that the complex sum only varies in phase (Fig. 26, circumferential line from grey circle).

The trends in Figs. 24 and 25 are projections of the two-dimensional complex sum onto magnitude and phase coordinates. For example, this explains why the maximum sensitivity of impedance phase occurs at the frequency where impedance magnitude is insensitive. The implication is that the effect of axial gap will be a strong function of frequency in any given case, and no universal conclusion may be drawn. However, the TAD model is a useful tool to analyse this effect in the general case.

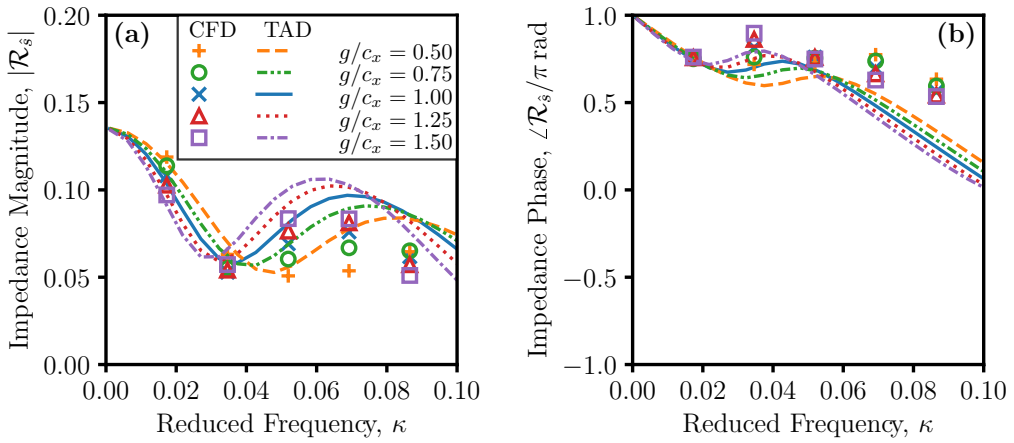

Figure 25: Effect of stator–rotor axial gap size on acoustic impedance of a turbine stage to convecting entropy wave, predicted by analytical model and CFD: **(a)** impedance magnitude, **(b)** impedance phase. The entropy-acoustic transfer function at $\kappa = 0.05$ doubles as gap increases by a factor of three.

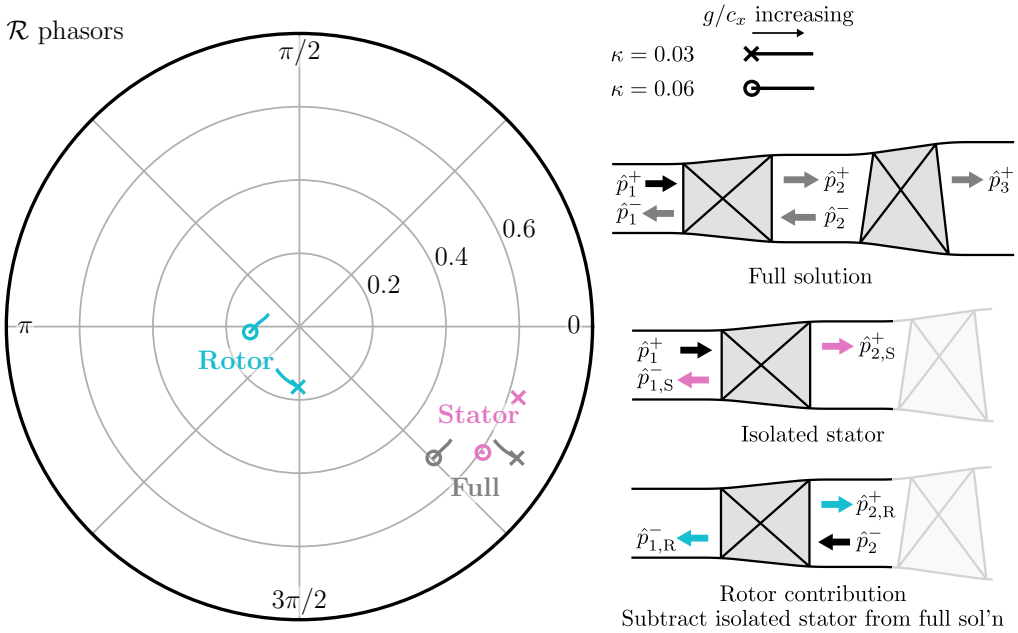

Figure 26: Effect of axial gap on stator and rotor contributions to turbine acoustic impedance, predicted by TAD model. At $\kappa = 0.03$ the relative phase of the contributions gives reduced impedance as gap increases. At $\kappa = 0.06$, the rotor contribution is phase-shifted and axial gap only alters impedance phase.

7. Physical mechanisms neglected by the analytical model

The literature has reported some physical mechanisms that are not included in the TAD analytical model. Various studies have demonstrated effects on acoustic impedance using their own analytical modelling or experimental measurements. This section considers the implications of those results for the present turbomachinery modelling approach. Non-planar entropy waves, non-isentropicity, vorticity noise and compositional noise will be discussed.

7.1. Non-planar entropy waves

The present method uses an empirical attenuation coefficient, calculated by convecting entropy waves along streamlines from three-dimensional CFD results, to approximate entropy wave dispersion within blade rows (Section 2.3). A limitation of this approach is that incident entropy waves are assumed planar upstream of each row.

In reality, entropy fluctuations are non-uniform over the turbine inlet. From large-eddy simulations of a combustion chamber, Livebardon et al. [26] found that the planar mode accounted for no more than 40% of the entropy fluctuation energy. Pinelli et al. [27] predicted a variation in upstream entropy noise power of up to 5.2dB when clocking unsteady hot spots with respect to the turbine.

Suppose the distribution of entropy fluctuations over the turbine inlet is known for a given combustor geometry. Assigning a different amplitude and phase to entropy waves on each streamline, dependent on the start location, will sensitise the attenuation coefficient to a distribution of non-planar entropy waves. This modification to the model is, however, unvalidated. Because entropy wave dispersion effects are specific to the detailed combustor and turbine flow field, a pragmatic approach would be to use higher-fidelity modelling later in the design cycle.

7.2. Non-isentropicity

De Domenico et al. [28] present entropy noise measurements for nozzles, and a non-isentropic analytical model that reproduces their experimental results. They use a non-isentropicty parameter, β, to characterise entropy rise or equivalently pressure loss. Maximum loss corresponds to an orifice plate, where $\beta < 1$ is equal to the orifice area ratio. $\beta = 1$ corresponds to isentropic flow. The convergent–divergent nozzle in their study is highly lossy, with $\beta \leq 0.032$.

In contrast, turbine blades are essentially convergent passages with lower levels of loss: for the first vane of the multi-stage turbine in this paper $\beta = 0.907$. The present model only captures non-isentropicity in the mean flow, conserving entropy in acoustic perturbations, but yields adequate agreement with CFD simulations. This suggests that non-isentropicity in the acoustic field may be neglected for representative high-efficiency turbine stages. Indeed, the non-isentropic model of De Domenico et al. [28] treats flow in the contracting part of the nozzle as isentropic.

7.3. Vorticity noise

Flames are commonly swirl-stabilised in gas turbine combustors, leading to the possibility of unsteady perturbations in vorticity convecting through the turbine and generating acoustic waves. Few publications are available on this indirect noise mechanism.

Generating axial vorticity by injecting an unsteady tangential mass flow upstream of a nozzle, Kings and Bake [29] measured an acoustic response that they identified as vorticity noise. However, Hirschberg et al. [30] attributed the sound generation to change in nozzle mass flow rate during injection.

Analytical studies by Duran et al. [31] and Dowling and Mahmoudi [3] show that the contribution of radial vorticity perturbations to indirect noise is at least one order of magnitude lower than entropic perturbations. There are no estimates available of the relative magnitudes of axial vorticity and entropy noise transfer functions.

Axial vorticity perturbations do not admit a simple analytical model, being inherently three-dimensional. Furthermore, the spatial distribution of vorticity on the inlet plane is specific to a particular combustor geometry. Acoustic impedances to vorticity waves are outside the scope of the present study; the importance of vorticity noise in representative gas turbine combustion systems remains an open research question.

7.4. Compositional noise

The contribution of chemical inhomogeneities to indirect noise, or compositional noise, was first identified by Ihme [4]. Incomplete mixing or unsteady reaction rate produces fluctuations in gas composition. Acceleration through a nozzle converts the chemical potential energy of a compositional inhomogeneity into acoustic energy. Rolland et al. [32] provided experimental confirmation of the phenomenon.

Using a limit case of constant chemical potential, Magri et al. [33] argued that the ratio of entropy noise to compositional noise is a constant, dependent on thermodynamic and compositional state, but independent of flow conditions. The vane transfer functions predicted by Giusti et al. [34] using a multi-species acoustic model support this view, where entropy and compositional transfer functions are related by a proportional scaling.

The present analytical model treats the working fluid as a single homogeneous species, and does not account for chemical inhomogeneity directly. Based on the results cited above, however, trends in compositional impedances as a function of turbine design will follow those of entropy impedances reported in this paper (with a constant of proportionality dependent on the working fluid).

8. Conclusions

This paper used a combination of time-marching CFD and analytical methods to determine the modelling requirements for predicting acoustic impedance of realistic turbines. For the three-dimensional multi-stage test case presented, the results show:

1. A cambered semi-actuator disk model predicts acoustic impedances to within 9% of non-linear time-marching CFD data for incident downstream-running pressure waves, and 14% for incident entropy waves;
2. When the acoustic impedance to plane waves is of interest, single-passage unsteady CFD simulations offer an order of magnitude reduction in computational cost, while producing results within 4.7% of a periodic-sector computation;
3. The influence of successive downstream turbine stages on acoustic impedance rapidly reduces. For the present case, modelling only the front two stages is sufficient to predict reflection coefficients for downstream-running pressure and entropy waves;
4. The acoustic impedance of a multi-stage turbine may be assumed constant during off-design operation. To a close approximation, a multi-stage turbine operates at constant corrected flow, which fixes Mach numbers and hence acoustic behaviour.

Next, the paper explored the three-dimensional turbine design space by applying both the validated modelling approaches to families of parametrically generated turbine stage geometries. These results show:

5. Acoustic impedance is insensitive to hub-to-tip radius ratio, meaning that the current two-dimensional analytical model is accurate even for high aspect ratio stages with $HTR = 0.6$. Radial variations in impedance are linear, so the impedance of a non-uniform flow is the same as that of the corresponding mixed-out average flow;
6. Front-loading turbine blades increases acoustic impedance, because the axial Mach number increases within the blade passage. For the turbine stage considered in this paper, the impedance of front-loaded blades is up to 51% higher, and aft-loaded blades up to 16% lower, compared to a datum quadratic camber line;
7. Stator–rotor axial gap affects acoustic impedance by changing the relative phase of reflections from vane and blade rows. Increasing the gap from $g/c_x = 0.5$ to $g/c_x = 1.5$ leads to variations in pressure impedance of up to $\pm 11\%$ at different frequencies, and first-order variations in the entropy–acoustic transfer function;

Overall, the paper has shown that a cambered semi-actuator disk model produces quantitatively accurate acoustic impedance predictions for realistic turbines. The TAD model consistently captures trends over a wide design and operating space. Accounting for axial non-compactness and chordwise non-uniform mean flow is sufficient to produce a tool that is broadly applicable, addressing the need for rapid assessment of turbine acoustic impedance in an iterative design process.

9. Acknowledgements

The author thanks Mitsubishi Heavy Industries for sponsoring this work, and in particular, Dr. S. Uchida, Mr. K. Saitoh, and Mr. T. Koda for their interest and support. The author is grateful to Dr. Tom Hynes for sharing his semi-actuator disk code, and to Dr. Graham Pullan for his helpful comments on the draft manuscript.

Appendix A. Mixed-out averaging procedure

This appendix defines the mixed-out averaging method used in this paper to derive representative point values from spatially varying two dimensional flow fields. The mixed-out state is a hypothetical, uniform state where the flow is allowed to reach equilibrium in an infinite frictionless duct of constant area. The state is derived by conserving mass, momentum, and energy.

Given a flow field over a constant-x plane with area A, the method seeks a uniform state, denoted by $\breve{\square}$ that satisfies,

$$\text{Mass:} \quad \iint_A \rho V_x \,\mathrm{d}A = \breve{\rho}\breve{V}_x A\,, \tag{A.1a}$$

$$\text{Axial momentum:} \quad \iint_A \Big(\rho V_x^2 + p\Big)\,\mathrm{d}A = \Big(\breve{\rho}\breve{V}_x^2 + \breve{p}\Big)A\,, \tag{A.1b}$$

$$\text{Angular momentum:} \quad \iint_A \rho V_x r V_\theta \,\mathrm{d}A = \breve{\rho}\breve{V}_x \breve{r}\breve{V}_\theta A\,, \tag{A.1c}$$

$$\text{Energy:} \quad \iint_A \rho V_x \Big(h_0 - r\Omega V_\theta\Big)\,\mathrm{d}A = \breve{\rho}\breve{V}_x \Big(\breve{h}_0 - \breve{r}\Omega\breve{V}_\theta\Big)A\,. \tag{A.1d}$$

In Eqns. (A.1), Ω is the angular velocity of the reference frame, h_0 is the stagnation enthalpy, and all other symbols have their usual meaning. The mixed-out radius $\breve{r}$ is taken as the mid-span location, and assuming parallel streamlines the mixed-out state has no radial velocity.

The total fluxes on the left-hand sides are directly evaluated from the non-uniform flow field. A fixed-point iteration gives the right-hand side solution. First, guess a value of mixed-out density, $\breve{\rho}$; then evaluate $\breve{V}_x$, $\breve{p}$, $\breve{V}_\theta$, and $\breve{h}_0$ in turn by rearranging Eqns. (A.1); and finally calculate an updated density guess, repeating until converged.

Any averaging process entails a loss of information, and does not preserve every integral flow property (total entropy flux increases by the mixed-out method). However, in the present work, processing the computations using a simpler area-weighted average yielded negligible change in the results. This suggests that, for the degrees of non-uniformity predicted in this study, the choice of averaging method is somewhat arbitrary.

Appendix B. Derivation of transfer matrices

This appendix presents derivations for the transfer matrices $\mathbf{T}_i$ that relate characteristic waves $\mathbf{y}$ upstream and downstream of the ith blade row according to,

$$\mathbf{y}_{i+1} = \mathbf{T}_i \mathbf{y}_i \,. \tag{B.1}$$

Appendix B.1 sets out the notation required, then Appendix B.2 derives the transfer matrix for a flat plate cascade, as an intermediate step, and Appendix B.3 extends the procedure to cambered blades.

Appendix B.1. Notation

The solution for of Eqn. (2) may be written as,

$$\frac{p'(x,t)}{p} = \mathbf{z}_p \cdot \Big(\boldsymbol{\beta}(x)\mathbf{y}\Big) \exp\left(2\pi \mathrm{i} f t\right) \,, \tag{B.2}$$

where,

- $\mathbf{z}_p$ is a column vector of weights that relate amplitudes of the four characteristic waves to the amplitude of perturbation in static pressure. The weights depend on the mean flow and perturbation frequency. There are analogous vectors for other flow quantities, such as stagnation temperature $\mathbf{z}_{T_0}$ or entropy $\mathbf{z}_s$;
- $\boldsymbol{\beta}(x)$ is a diagonal matrix comprising terms like $\exp \beta x/r$ that govern decay of characteristic waves over axial distance within a control volume. The β decay factors, different for each characteristic wave type, are functions of the mean flow and perturbation frequency;
- $\mathbf{y} = [\hat{p}^-, \hat{p}^+, \hat{v}, \hat{s}]^{\mathrm{t}}$ is a column vector of characteristic wave amplitudes at the inlet of a control volume. The solution for $\mathbf{y}$ depends on the imposed unsteadiness or non-uniformity at boundaries of the machine, and indirectly depends on the mean flow via the $\mathbf{z}$ and $\boldsymbol{\beta}(x)$ terms;

After evaluating the weights $\mathbf{z}$ and decay rates $\boldsymbol{\beta}(x)$ from the mean flow and perturbation parameters [7, 10], the task is to determine the four characteristic wave amplitudes $\mathbf{y}$ that result from given boundary conditions.

The corresponding form for the solution in blade passages is,

$$\frac{\tilde{p}'(x,t)}{\tilde{p}} = \tilde{\mathbf{z}}_p \cdot \Big(\tilde{\boldsymbol{\beta}}(x)\tilde{\mathbf{y}}\Big) \exp\left(2\pi \mathrm{i} f t\right) \,, \tag{B.3}$$

analogous to Eqn. (B.2), where a tilde distinguishes passage quantities from their annulus counterparts.

Appendix B.2. Flat plate transfer matrix

First assemble weight vectors into matrices that convert characteristic waves to flow quantities of interest in the annulus control volumes,

$$\mathbf{F} = \begin{bmatrix} \leftarrow \mathbf{z}^{\mathrm{t}}_{\rho V_x} \rightarrow \\ \leftarrow \mathbf{z}^{\mathrm{t}}_{T_0} \rightarrow \\ \leftarrow \mathbf{z}^{\mathrm{t}}_{s} \rightarrow \end{bmatrix} \quad \text{and} \quad \mathbf{G} = \begin{bmatrix} \leftarrow \mathbf{z}^{\mathrm{t}}_{\rho V_x} \rightarrow \\ \leftarrow \mathbf{z}^{\mathrm{t}}_{T_0} \rightarrow \\ \leftarrow \mathbf{z}^{\mathrm{t}}_{p_0} \rightarrow \\ \leftarrow \mathbf{z}^{\mathrm{t}}_{\alpha} \rightarrow \end{bmatrix} . \tag{B.4}$$

Multiplying the characteristic wave vector by the conversion matrices, and denormalising using mean flow quantities yields dimensional values of the conserved quantities. At the leading edge (LE) of the ith blade row,

$$\begin{bmatrix} (\rho V_x)' \\ T_0' \\ s' \end{bmatrix}_{i,\mathrm{LE}} = \begin{bmatrix} \rho V_x & 0 & 0 \\ 0 & T_0 & 0 \\ 0 & 0 & s \end{bmatrix}_i \mathbf{F}_i \boldsymbol{\beta}_i(l_i) \mathbf{y}_i \ , \tag{B.5}$$

where the $\boldsymbol{\beta}_k(l_i)$ term accounts for decay of characteristic waves from the inlet of the ith control volume, the defining location for $\mathbf{y}_k$, to the leading edge of the ith blade row over a distance l_i. Similarly, for the ith passage trailing edge (TE),

$$\begin{bmatrix} (\rho V_x)' \\ T_0' \\ p_0' \\ \alpha' \end{bmatrix}_{i,\mathrm{TE}} = \begin{bmatrix} \rho V_x & 0 & 0 & 0 \\ 0 & T_0 & 0 & 0 \\ 0 & 0 & p_0 & 0 \\ 0 & 0 & 0 & 1 \end{bmatrix}_{i+1} \mathbf{G}_{i+1} \boldsymbol{\beta}_{i+1}(0) \mathbf{y}_{i+1} \ , \tag{B.6}$$

where $\boldsymbol{\beta}_{i+1}(0) = \mathbf{I}$ as the passage trailing edge is coincident with the next control volume inlet.

Similar expressions to Eqns. (B.4) evaluate the perturbations in conserved quantities from the characteristic waves inside the blade passage,

$$\tilde{\mathbf{F}}_i = \begin{bmatrix} \leftarrow \tilde{\mathbf{z}}^{\mathrm{t}}_{\rho V_x} \rightarrow \\ \leftarrow \tilde{\mathbf{z}}^{\mathrm{t}}_{T_0} \rightarrow \\ \leftarrow \tilde{\mathbf{z}}^{\mathrm{t}}_{s} \rightarrow \end{bmatrix}_i \quad \text{and} \quad \tilde{\mathbf{G}}_i = \begin{bmatrix} \leftarrow \tilde{\mathbf{z}}^{\mathrm{t}}_{\rho V_x} \rightarrow \\ \leftarrow \tilde{\mathbf{z}}^{\mathrm{t}}_{T_0} \rightarrow \\ \leftarrow \tilde{\mathbf{z}}^{\mathrm{t}}_{p_0} \rightarrow \\ \leftarrow \mathbf{0} \rightarrow \end{bmatrix}_i . \tag{B.7}$$

The perturbations just inside the ith passage at leading and trailing edges are,

$$\begin{bmatrix} (\rho V_x)' \\ T_0' \\ s' \end{bmatrix}_{i,\widetilde{\mathrm{LE}}} = \begin{bmatrix} \widetilde{\rho V_x} & 0 & 0 \\ 0 & \widetilde{T_0} & 0 \\ 0 & 0 & \widetilde{s} \end{bmatrix}_i \tilde{\mathbf{F}}_i \tilde{\boldsymbol{\beta}}_i(0) \tilde{\mathbf{y}}_i \ , \tag{B.8}$$

and,

$$\begin{bmatrix} (\rho V_x)' \\ T_0' \\ p_0' \\ \alpha' \end{bmatrix}_{i,\widetilde{\mathrm{TE}}} = \begin{bmatrix} \widetilde{\rho V_x} & 0 & 0 & 0 \\ 0 & \widetilde{T_0} & 0 & 0 \\ 0 & 0 & \widetilde{p_0} & 0 \\ 0 & 0 & 0 & 1 \end{bmatrix}_i \tilde{\mathbf{G}}_i \tilde{\boldsymbol{\beta}}_i(c_i) \tilde{\mathbf{y}}_i \ , \tag{B.9}$$

where the $\tilde{\boldsymbol{\beta}}_k(c_i)$ term accounts for decay of characteristic waves along the chord.

Enforcing boundary conditions at the leading edge requires that the right-hand sides of Eqns. (B.5) and (B.8) are equal,

$$\mathbf{F}_i \boldsymbol{\beta}_i(l_i)\mathbf{y}_i = \tilde{\mathbf{F}}_i \tilde{\boldsymbol{\beta}}_i(0)\tilde{\mathbf{y}}_i \ , \tag{B.10}$$

using the fact that the mean flow mass flux, stagnation temperature, and entropy are all continuous at the leading edge, for example, $\rho V_x = \widetilde{\rho V_x}$. At the trailing edge, the right-hand sides of Eqns. (B.6) and (B.9) are equal,

$$\mathbf{Q}_i \mathbf{G}_{i+1} \boldsymbol{\beta}_{i+1}(0)\mathbf{y}_{i+1} = \tilde{\mathbf{G}}_i \tilde{\boldsymbol{\beta}}_i(c_i)\tilde{\mathbf{y}}_i \ , \tag{B.11}$$

where

$$\mathbf{Q}_i = \begin{bmatrix} \dfrac{(\rho V_x)_{i+1}}{\widetilde{(\rho V_x)_i}} & 0 & 0 & 0 \\ 0 & \dfrac{T_{0,i+1}}{\widetilde{T}_{0,i}} & 0 & 0 \\ 0 & 0 & \dfrac{p_{0,i+1}}{\widetilde{p}_{0,i}} & 0 \\ 0 & 0 & 0 & 1 \end{bmatrix} \ , \tag{B.12}$$

is a diagonal matrix that accounts for discontinuity in mean flow, due to stagnation pressure losses within blade rows or injection of coolant. Eliminating $\tilde{\mathbf{y}}_i$ from Eqns. (B.10) and (B.11), and noting that $\boldsymbol{\beta}(0) = \mathbf{I}$, gives an expression for the transfer matrix,

$$\mathbf{y}_{i+1} = \underbrace{\left[\mathbf{Q}_i \mathbf{G}_{i+1}\right]^{-1} \tilde{\mathbf{G}}_i \tilde{\boldsymbol{\beta}}_i(c_i) \tilde{\mathbf{F}}_i^{-1} \mathbf{F}_i \boldsymbol{\beta}_i(l_i)}_{\text{flat plate transfer matrix } \mathbf{T_i}} \mathbf{y}_i \ . \tag{B.13}$$

Appendix B.3. Cambered blade transfer matrix

The analytical model splits a cambered blade into $j = 1, ..., N_j$ flat-plate elements, of equal axial length $\Delta x_i = c_i/N_j$. Each element has a different mean flow and hence $\tilde{\mathbf{F}}_{i,j}$ and $\tilde{\mathbf{y}}_{i,j}$ vary through the passage. Applying the leading edge continuity conditions to all the splits between elements yields the set of equations,

$$\begin{aligned} \text{LE} \leftrightarrow 1: \quad & \mathbf{F}_i \boldsymbol{\beta}_i(l_i)\mathbf{y}_i = \tilde{\mathbf{F}}_{i,1} \tilde{\boldsymbol{\beta}}_{i,1}(0)\tilde{\mathbf{y}}_{i,1} \ , \\ 1 \leftrightarrow 2: \quad & \tilde{\mathbf{F}}_{i,1} \tilde{\boldsymbol{\beta}}_{i,1}(\Delta x_i)\tilde{\mathbf{y}}_{i,1} = \tilde{\mathbf{F}}_{i,2} \tilde{\boldsymbol{\beta}}_{i,2}(0)\tilde{\mathbf{y}}_{i,2} \ , \\ & \cdots \\ N_j - 1 \leftrightarrow N_j: \quad & \tilde{\mathbf{F}}_{i,N_j-1} \tilde{\boldsymbol{\beta}}_{i,N_j-1}(\Delta x_i)\tilde{\mathbf{y}}_{i,N_j-1} = \tilde{\mathbf{F}}_{i,N_j} \tilde{\boldsymbol{\beta}}_{i,N_j}(0)\tilde{\mathbf{y}}_{i,N_j} \ , \\ N_j \leftrightarrow \text{TE}: \quad & \tilde{\mathbf{G}}_{i,N_j} \tilde{\boldsymbol{\beta}}_{i,N_j}(\Delta x_i)\tilde{\mathbf{y}}_{i,N_j} = \mathbf{Q}_i \mathbf{G}_{i+1} \boldsymbol{\beta}_{i+1}(0)\mathbf{y}_{i+1} \ . \end{aligned} \tag{B.14}$$

Eliminating all the $\tilde{\mathbf{y}}_{i,j}$ from the system of Eqns. (B.14), and putting $\tilde{\boldsymbol{\beta}}_{i,j}(0) = \mathbf{I}$, yields the transfer matrix for a cambered blade,

$$\mathbf{T}_i = \left[\mathbf{Q}_i \mathbf{G}_{i+1}\right]^{-1} \tilde{\mathbf{G}}_{i,N_j} \tilde{\boldsymbol{\beta}}_{i,N_j}(\Delta x_i) \tilde{\mathbf{F}}_{i,N_j}^{-1} \left[\prod_{j=N_j-1}^{1} \tilde{\mathbf{F}}_{i,j} \tilde{\boldsymbol{\beta}}_{i,j}(\Delta x_i) \tilde{\mathbf{F}}_{i,j}^{-1} \right] \mathbf{F}_i \boldsymbol{\beta}_i(l_i) \ . \tag{B.15}$$

References

[1] A. Dowling, The calculation of thermoacoustic oscillations, J. Sound Vib. 180 (1995) 557–581.

[2] T. Poinsot, Prediction and control of combustion instabilities in real engines, Proc. Combust. Inst. 36 (2017) 1 – 28.

[3] A. P. Dowling, Y. Mahmoudi, Combustion noise, Proc. Combust. Inst. 35 (2015) 65–100.

[4] M. Ihme, Combustion and engine-core noise, Annu. Rev. Fluid Mech. 49 (2017) 277–310.

[5] M. P. Juniper, R. Sujith, Sensitivity and Nonlinearity of Thermoacoustic Oscillations, Annu. Rev. Fluid Mech. 50 (2018) 661–689.

[6] F. Marble, S. Candel, Acoustic disturbance from gas non-uniformities convected through a nozzle, J. Sound Vib. 55 (1977) 225–243.

[7] N. A. Cumpsty, F. E. Marble, The Interaction of Entropy Fluctuations with Turbine Blade Rows: A Mechanism of Turbojet Engine Noise, Proc. Roy. Soc. London 357 (1977) 323–344.

[8] M. Leyko, I. Duran, S. Moreau, F. Nicoud, T. Poinsot, Simulation and modelling of the waves transmission and generation in a stator blade row in a combustion-noise framework, J. Sound Vib. 333 (2014) 6090–6106.

[9] A. Mishra, D. J. Bodony, Evaluation of actuator disk theory for predicting indirect combustion noise, J. Sound Vib. 332 (2013) 821–838.

[10] M. Bauerheim, I. Duran, T. Livebardon, G. Wang, S. Moreau, T. Poinsot, Transmission and reflection of acoustic and entropy waves through a stator–rotor stage, J. Sound Vib. 374 (2016) 260–278.

[11] S. Kaji, T. Okazaki, Propagation of sound waves through a blade row: I. Analysis based on the semi-actuator disk theory, J. Sound Vib. 11 (1970) 339–353.

[12] S. Kaji, T. Okazaki, Propagation of sound waves through a blade row: II. Analysis based on the acceleration potential method, J. Sound Vib. 11 (1970) 355–IN1.

[13] J. Brind, G. Pullan, Modelling Turbine Acoustic Impedance, Int. J. Turbomach. Propuls. Power 6 (2021).

[14] D. Papadogiannis, G. Wang, S. Moreau, F. Duchaine, L. Gicquel, F. Nicoud, Assessment of the Indirect Combustion Noise Generated in a Transonic High-pressure Turbine Stage, J. Eng. Gas Turbines Power 138 (2016).

[15] A. Giusti, N. A. Worth, E. Mastorakos, A. P. Dowling, Experimental and Numerical Investigation into the Propagation of Entropy Waves, AIAA J. 55 (2017) 446–458.

[16] L. Cremer, The treatment of fans as black boxes, J. Sound Vib. 16 (1971) 1–15.

[17] J. D. Denton, Multall—An Open Source, Computational Fluid Dynamics Based, Turbomachinery Design System, J. Turbomach 139 (2017) 121001.

[18] J. D. Denton, The Calculation of Three-Dimensional Viscous Flow Through Multistage Turbomachines, J. Turbomach 114 (1992) 18–26.

[19] T. Brandvik, G. Pullan, An Accelerated 3D Navier–Stokes Solver for Flows in Turbomachines, J. Turbomach. 133 (2011) 021025.

[20] T. Poinsot, C. Le Chatelier, S. Candel, E. Esposito, Experimental determination of the reflection coefficient of a premixed flame in a duct, J. Sound Vib. 107 (1986) 265–278.

[21] A. Emmanuelli, J. Zheng, M. Huet, A. Giauque, T. Le Garrec, S. Ducruix, Description and application of a 2d-axisymmetric model for entropy noise in nozzle flows, J. Sound Vib. 472 (2020) 115163.

[22] N. A. Cumpsty, Jet Propulsion, 2nd ed., Cambridge University Press, 2003.

[23] S. Dixon, C. Hall, Fluid Mechanics and Thermodynamics of Turbomachinery, 7th ed., Elsevier, 2014.

[24] R. J. Howell, O. N. Ramesh, H. P. Hodson, N. W. Harvey, V. Schulte, High Lift and Aft-Loaded Profiles for Low-Pressure Turbines , J. Turbomach 123 (2001) 181–188.

[25] G. Pullan, J. Denton, E. Curtis, Improving the Performance of a Turbine With Low Aspect Ratio Stators by Aft-Loading, J. Turbomach. 128 (2004) 492–499.

[26] T. Livebardon, S. Moreau, L. Gicquel, T. Poinsot, E. Bouty, Combining LES of combustion chamber and an actuator disk theory to predict combustion noise in a helicopter engine, Combust. Flame 165 (2016) 272–287.

[27] L. Pinelli, M. Marconcini, R. Pacciani, F. Bake, K. Knobloch, P. Gaetani, G. Persico, Effect of clocking on entropy noise generation within an aeronautical high pressure turbine stage, J. Sound Vib. 529 (2022) 116900.

[28] F. De Domenico, E. O. Rolland, J. Rodrigues, L. Magri, S. Hochgreb, Compositional and entropy indirect noise generated in subsonic non-isentropic nozzles, J. Fluid Mech. 910 (2021) A5.

[29] N. Kings, F. Bake, Indirect combustion noise: Noise generation by accelerated vorticity in a nozzle flow, Int. J. Spray Combust. Dyn. 2 (2010) 253–266.
[30] L. Hirschberg, S. J. Hulshoff, F. Bake, Sound production due to swirl–nozzle interaction: Model-based analysis of experiments, AIAA J. 59 (2021) 1269–1276.
[31] I. Duran, S. Moreau, F. Nicoud, T. Livebardon, E. Bouty, T. Poinsot, Combustion noise in modern aero-engines, AerospaceLab J. Issue 7 (2014) 1–11.
[32] E. O. Rolland, F. D. Domenico, S. Hochgreb, Direct and indirect noise generated by entropic and compositional inhomogeneities, J. Eng. Gas Turbines Power 140 (2018).
[33] L. Magri, J. O'Brien, M. Ihme, Compositional inhomogeneities as a source of indirect combustion noise, J. Fluid Mech. 799 (2016).
[34] A. Giusti, L. Magri, M. Zedda, Flow inhomogeneities in a realistic aeronautical gas-turbine combustor: Formation, evolution, and indirect noise, J. Eng. Gas Turbines Power 141 (2018) 011502.